

This is a preprint of the following article, which is available from mdolab.engin.umich.edu and www.researchgate.net

@Article{Anibal2022, author = Joshua Anibal and Charles A. Mader and Joaquim R. R. A. Martins, title = Aerodynamic shape optimization of an electric aircraft motor surface heat exchanger with conjugate heat transfer constraint, doi = 10.1016/j.ijheatmasstransfer.2022.122689, journal = International Journal of Heat and Mass Transfer, month = June, pages = 122689, volume = 189, year = 2022 }

The original article may differ from this preprint and is available at

<https://doi.org/10.1016/j.ijheatmasstransfer.2022.122689>.

Aerodynamic shape optimization of an electric aircraft motor surface heat exchanger with conjugate heat transfer constraint

Joshua L. Anibal¹, Charles A. Mader, Joaquim R. R. A. Martins

University of Michigan, Ann Arbor, Michigan

Abstract

Electrified aircraft benefit from the versatile ways electric motors can be integrated with an airframe. However, thermal management is needed to move waste heat out of the motors because the heat is not expelled with the exhaust as in a conventional engine. Plate-fin, fin, and surface heat exchangers are incorporated as air-side heat exchangers for electrified aircraft thermal management systems. Typically, analytic tools are used to design heat exchangers within these categories. However, analytic tools lack the fidelity required for detailed shaping and assessment of general heat exchanger configurations. Tools based on first principles, such as finite element analysis or computational fluid dynamics, can verify heat exchanger performance but are too costly to use in a manual design loop. Shape optimization can be used with first-principles-based models to design heat exchangers without limiting the geometry to those previously well studied. In this work, we apply this methodology to design a heat sink for the high-lift motor of an electric technology demonstrator, the X-57 Maxwell. We use a gradient-based optimizer to modify the thickness distribution of the heat sink to find designs that minimize drag while meeting the heat load constraint. To model the heat transfer from the motor, we use both convection-only and conjugate heat transfer models and compare the resulting differences in the optimized shapes. We found that the convection-only model under-predicted heat rejection and thus led to larger than necessary heat sinks when used in optimization. To study the effect of the heat load on the design, we compare the heat sinks designed for the baseline motor and heat sinks designed for less efficient motors. Our study results show how the heat exchanger's geometry changes from uniformly thick to designs with fins as the heat load

increases. Furthermore, we found that the variation in drag across designs is driven by differences in the pressure drag due to flow separation. Finally, we conclude with a comparison of the optimized designs to those representing more simple fin designs and find that the optimized designs have fins that are shifted forward to reduce the adverse pressure gradient, which mitigates separation on the aft part of the fin. The developed shape optimization method could also be applied to improve other heat exchangers, specifically those designed to reject relatively low amounts of heat.

1 Introduction

Aircraft electrification acts as a method to reduce the carbon footprint of current aircraft operations and is an enabling technology for new missions. Aircraft electrification encompasses full-electric, turboelectric, series hybrid, and parallel hybrid aircraft. A common thread in all these modes of electrification is the use of electric motors. Electric motors offer an emission-free alternative to current gas-powered propulsion. Additionally, the scale-independent efficiency of electric motors enables a wide variety of new aircraft concepts [Brelje and Martins \(2019\)](#). These new aircraft concepts integrate electric motors with the airframes in novel ways to produce net aeropropulsive benefits. These concepts include the use of large tail-mounted propulsors to ingest significant portions of the boundary layer like the NASA STARC-ABL [Welstead and Felder \(2016\)](#) and Airbus Volt Air [Stückl et al. \(2012\)](#). Other concepts ingest the boundary layer using a distributed set of small propulsors such as the NASA N3-X [Jansen et al. \(2017\)](#) [Armstrong et al. \(2012\)](#). Sets of small propulsors can also be positioned on the leading edge of a wing to increase its maximum lift. This is exemplified by NASA’s electric aircraft technology demonstrator, the X-57 Maxwell. During takeoff and landing, the X-57 uses an additional set of motors distributed along the wing to bolster the high-lift performance of its reduced size wing [Borer et al. \(2016\)](#).

However, using electric motors in aircraft brings about new challenges. Waste heat produced by motors and related power electronics must be managed despite the high efficiency of electric motors ($\approx 95\%$). This is because losses in the motor generate waste heat inside the motor itself, unlike conventional aircraft propulsion, where the waste heat is naturally expelled with the exhaust. Inadequate thermal management of this waste heat leads to reduced motor performance, degradation of magnets and other critical components, and motor failure. To mitigate these issues, electric aircraft need to limit the waste heat they produce to the amount that the thermal management system can reject. [Falck et al. \(2017\)](#) have shown that for optimal trajectories of the X-57 mod III, the rate of climb must be limited to prevent the buildup of excess waste heat.

1.1 Heat exchangers for electric motors

To facilitate the rejection of heat into the atmosphere, thermal management systems incorporate air-side heat exchangers. A varied set of heat exchangers are used for electrified aircraft because of the range of motor and electrical component sizes and the varied ways they are integrated with the aircraft.

Plate-fin heat exchangers are common in aerospace applications because of their compactness and low weight [Sundén and Fu \(2017\)](#). These heat exchangers move heat into ducted air from another cooling fluid. The NASA turboelectric VTOL concept uses this type of heat exchanger [Chapman et al. \(2020\)](#). Although this type of heat exchanger effectively rejects large quantities of heat, it also requires pumps and coolant. If cooling power is needed at low flight speeds, a puller fan may also be required to move the required amount of air through the heat exchanger. As a result, the plate-fin design is more practical at larger scales where the weight penalties of the pumps, coolant, and puller fan have a smaller relative impact. Additionally, the plate-fin design works well when another liquid on the aircraft can serve as the working fluid of the heat exchanger as well, such as the oil or fuel in a turboelectric design.

Finned heat exchangers, also called heat sinks, consist of a single layer of fins joined by a base. These heat exchangers can be placed directly in the freestream or use ducted air to move air around the fins. As shown in Figure 1a, the Airbus A³ Vahana aircraft prototype used fins attached directly to its motors and placed in the propeller slipstream [S.A.S. \(2021\)](#). Fin heat exchangers are well suited for small heat loads, and for heat sources positioned close to the surface.

The aircraft’s surface can also be used as a heat exchanger without adding any additional structures. [Sozer et al. \(2020\)](#) investigated the use of surface heat exchangers for a single-aisle turboelectric concept (STARC-ABL), turboelectric VTOL concept, and hybrid electric regional aircraft concept (PEGASUS). [Schnulo et al. \(2020\)](#) further investigated the impact of the surface heat exchangers on the fuel burn of the STARC-ABL concept with an advanced power system and found that it reduced fuel burn by an additional 0.8% and removed the complexity of the pumps and coolant system. The first concept of the Alice aircraft by Eviation had wingtip motors that moved heat to the streamlined surface of the nacelle where it was convected away [Zivan \(2019\)](#). Another example of an electric aircraft that uses this basic form of a heat exchanger is the aircraft concept by iSight of Fraunhofer, which mounts the hot motor controller components directly on the motor nacelle [Bentheimer et al. \(2019\)](#). The X-57 high lift motor also uses this method to cool both the high lift motors and their motor controllers [Hall et al. \(2019\)](#). Figure 1b displays the surface heat exchanger of the high-lift motor as shown by [Hall et al. \(2019\)](#). [Kellermann et al. \(2020\)](#) note that the challenges of surface heat exchangers include a lower availability of cooling power at slow flight speeds. Surface heat exchangers are well suited for applications that require low amounts of cooling power and prioritize a clean low-drag surface. In another work, [Kellermann et al. \(2019\)](#) highlight the potential of surface heat exchangers for aircraft and note that smaller aircraft would benefit most from this kind of cooling.

1.2 Design of heat exchangers for electric motors

Typically, engineers use analytic equations to compare across categories of heat exchangers and for rough-sizing optimizations, while high-fidelity simulations are used for manual design and verification. Plate-fin, finned, and flat surface heat exchangers have been well studied, and equations for their sizing and performance are provided in classical texts [Shah and Sekulić \(2003\)](#); [Kays and London \(1998\)](#). Once sized, a



(a) Airbus A³ Vahana motor heat exchanger [S.A.S. \(2021\)](#).



(b) X-57 surface heat exchanger (black region) [Hall et al. \(2019\)](#).

Figure 1: Examples of electric aircraft heat exchangers.

comparison between categories can be made with the rough performance estimates of each type. [Chapman et al. \(2020\)](#) utilized this approach to optimize the length, width, and height of the layers in a plate-fin heat exchanger to find a set of Pareto optimal designs with respect to weight and power. Similarly, [Kellermann et al. \(2020\)](#) varied the hydraulic diameter of a plate-fin heat exchanger and resized the entire thermal management system to find the optimum design. In another work, [Kellermann et al. \(2019\)](#) used flat plate heat transfer correlations to assess the potential of surface heat exchangers as a function of aircraft size.

Analytic calculations are suitable for fins, radiators, and flat surfaces, but are not as insightful for designs that cannot be well-defined by these geometries. This restricts the designs that can be produced from analytical equations to designs that have been previously extensively studied, limiting the discovery of more performant concepts. For the design of nontraditional heat exchangers, first-principles-based simulation is needed. High-fidelity simulation tools can evaluate performance but are costly to iterate with by hand. [Hall et al. \(2019\)](#) use high-fidelity simulation to verify the surface heat exchanger would be sufficient, but do not use it as part of a design loop. Optimization alleviates this issue by automating the process of design refinement. As a result, optimization provides a way to use high-fidelity simulation tools to design more performant heat exchangers.

1.3 Shape optimization in heat transfer

Shape optimization can be used with first-principles heat transfer models to design parts that reject heat more efficiently. The design optimization work for heat transfer primarily focuses on gradient-free methods [Gosselin et al. \(2009\)](#); [Fabbri \(2000\)](#); [Dennis et al. \(2003\)](#); [Mazaheri et al. \(2016\)](#). However, shape optimization applications require many design variables to parameterize the broad range of surface shapes. Additionally, to distinguish the performance of two slightly different surface shapes, expensive

detailed analysis is often required. Unfortunately, when using gradient-free methods, the number of function evaluations increases quickly as the number of design variables increases (Martins and Ning, 2022, ch 7.). This makes gradient-free methods ill-suited for aerodynamic shape optimization problems, which have many design variables and expensive function evaluations Yu et al. (2018). Gradient-based methods, on the other hand, have much better scalability and thus are well suited for shape optimization problems Lyu et al. (2014). The following research has extended the use of gradient-based optimization problems to include conduction, convection, and conjugate heat transfer models.

1.3.1 Conduction

Gradient-based shape optimization has been used with conduction models to design parts that optimally conduct heat. Katamine et al. (2013) performed shape optimization on a test problem with a temperature-dependent thermal conductivity coefficient. Wang et al. (2017); Li and Qian (2011); Yoon et al. (2013), and Meric (1998) highlighted the use of isogeometric approaches in the shape optimization of solid bodies that conduct heat. To minimize the variation of temperature within a solid body heated by an electrical current from the target temperature, Meric (1998) used a conjugate gradient method to vary the shape of the solid. Kambampati et al. (2019) used a conduction model to add temperature constraints and thermal loads to a set of compliance, mass, and stress minimization topology optimization problems. Leader and Kennedy (2021) performed topology optimization with steady-state and transient conduction analysis and found that the transient results differed from the steady-state result but converged to the steady-state result as the transient time interval was increased. For a detailed overview of topology optimization results using conduction models, see section 4.3 of the review by Dbouk (2017).

1.3.2 Convection

Forced convection models have been used in gradient-based optimization to optimize parts that reject heat into a moving fluid or are heated by a moving fluid. A major application of these works has been the shape optimization of jet engine turbine blades. Mousavi and Nadarajah (2010) used a 2D Navier–Stokes convection model to compute the temperature gradient on the blade surface and minimize it with respect to the geometry mesh points and the blade cooling holes. Likewise, Zhang et al. (2017) used a 2D Reynolds-averaged Navier–Stokes (RANS) and Spalart–Allmaras (SA) turbulence model to minimize the entropy generation with respect to shape variables for the suction side of the turbine blade, leading to a reduction in heat transfer for the isothermal wall condition. The design of the turbine blade internal passages has also been an area of focus for gradient-based shape optimization with convective heat transfer. Using a model of 3D RANS with an SA turbulence model, He et al. (2019) found a set of Pareto optimal designs for pressure loss and heat transfer for both a smooth and ribbed U-bend passageway. There have also been efforts to optimize the shape of finned heat exchangers with gradient-based algorithms and convection models. Wang et al. (2015) optimized the length, width, height, and pitch of the fins in a fin heat

exchanger to minimize a composite objective function of heat transfer and pressure loss. Similarly, [Gkaragkounis et al. \(2018\)](#) used volumetric B-splines to warp a cooling fin to either minimize pressure loss or maximize temperature. [Mario et al. \(2021\)](#) used adjoint-based topology optimization to minimize a weighted objective function of pressure loss and heat transfer for a 2D representation of the fins in a plate-fin heat exchanger. For a detailed overview of topology optimization using convection models, see section 4.4 of the review by [Dbouk \(2017\)](#).

1.3.3 Conjugate

A smaller set of work uses conjugate heat transfer models in gradient-based shape optimization. Conjugate heat transfer is the transport of heat through a combination of conduction and convection (see Section 2.4 for more detail). To maximize the heat transfer rate of a 2D turbine blade, [Mazaheri et al. \(2016\)](#) used a conjugate heat transfer model with variables to modify the internal cooling passages. [Mousavi and Nadarajah \(2011\)](#) built on their prior work and incorporated a conjugate heat transfer model to optimize turbine blade geometry as well as the location and angle of injection of the cooling holes. [Gkaragkounis et al. \(2018\)](#) modified the shape of a turbine blade as well as the position of cooling holes to minimize the average temperature in the blade. [Racca et al. \(2020\)](#) altered shape parameters to minimize the stress in radial turbine impeller blades with thermomechanical loads computed using a conjugate heat transfer model to find the internal temperature of the blades. [Sandboge et al. \(2021\)](#) used shape variables to modify the inlet and outlet in a battery pack to reduce the maximum internal battery temperature. [Gkaragkounis et al. \(2020\)](#) showed that the grid displacement algorithm had no significant effect on the optimized shape of the channel heat exchanger analyzed using conjugate heat transfer. [Gkaragkounis et al. \(2021\)](#) used volume b-splines to change the external and internal shape of a fin heat exchanger to find the set of Pareto optimal designs with respect to pressure loss and the minimization of the high-temperature areas over the solid domain. [Papoutsis-Kiachagias and Giannakoglou \(2020\)](#) used adjoint-based topology optimization to find a set of Pareto optimal designs of a micro-channel heat exchanger modeled with conjugate heat transfer. Additionally, [Makhija and Beran \(2019\)](#) have explored the optimization of surface shape and internal topology of the material distribution to maximize the average temperature of a cylinder subject to constraints. For a detailed overview of topology optimization using conjugate models, see section 4.6 of the review by [Dbouk \(2017\)](#).

1.4 Objective

Despite the prior work on high-fidelity shape optimization, there remains a need to apply these techniques to the design of electric aircraft heat exchangers. Additionally, there remains a need to study the trade-offs in the design of optimal electric aircraft surface heat exchangers. Lastly, the prior work does not compare the shapes of an electric aircraft heat exchanger optimized using convective and conjugate heat transfer models.

To address these needs, we build upon our prior work [Anibal et al. \(2020\)](#) to perform aerodynamic shape optimization of an electric aircraft heat exchanger. Furthermore, we use both convective and conjugate heat transfer models to minimize the drag of a surface heat exchanger for a range of heat transfer constraint values. The remainder of this paper has the following structure. In section 2.1 we describe the nacelle geometry of the X-57 high-lift motor, which is used as the baseline geometry of this study. Then, section 2.2 describes how the component models are combined to form a complete model of the heat exchanger’s performance. Next, the methodology for the aerodynamic model and the convection, conduction, and conjugate heat transfer models are laid out in sections 2.3, 2.4.2, 2.4.5, and 2.4.4, respectively. The following section, Section 2.5, is used to describe the methods for derivative calculations and the verification of their accuracy. Afterward, Section 2.7 lays out the optimization problem addressed in detail. In particular, it highlights how a free-form deformation technique is used to parametrize the nacelle’s outer mold line and the heat sink’s internal thickness distribution. Furthermore, this section details the choice of objective and constraint functions and how the values of the constraints were chosen. Finally, the results and discussion section, Section 3, details the outcome of solving the optimization problems. Discussion of the key results of this article are presented in the results and discussion section and then reiterated in the conclusion.

2 Methods

2.1 Nacelle geometry

We selected a simplified version of the X-57 high-lift motor nacelles as the baseline geometry of this study. During takeoff and landing, the X-57 uses its twelve high-lift motors for additional thrust and improved maximum lift. The motors connect directly to a heat sink that distributes heat across the surface of the motor nacelle’s outer mold line where it is rejected to the environment. The heat sink is required to dissipate heat because of the high power density of the motors, 4.95 kW/kg [Hall et al. \(2019\)](#). There is another fairing at the rear of the nacelle that houses the power electronics and wing attachment mechanism. The front of the nacelle geometry has a set of foldable propeller blades, which are pushed back against the nacelle by drag when not in use. The foldable propellers are attached to a hub that is covered by a spinner to reduce drag. In addition to being separated from the wing, the foldable propellers have been removed to simplify the geometry. The simplified geometry is shown in Figure 2 with the heat sink highlighted in red.

2.2 Model

The overall model incorporates components for altering the geometry according to design variables and a heat transfer and aerodynamic analysis to compute the drag and total heat transfer rate of the candidate design. The whole model is created by building and combining components in OpenMDAO [Gray et al. \(2019\)](#). In OpenMDAO, a component converts inputs to outputs and can represent an analysis or smaller

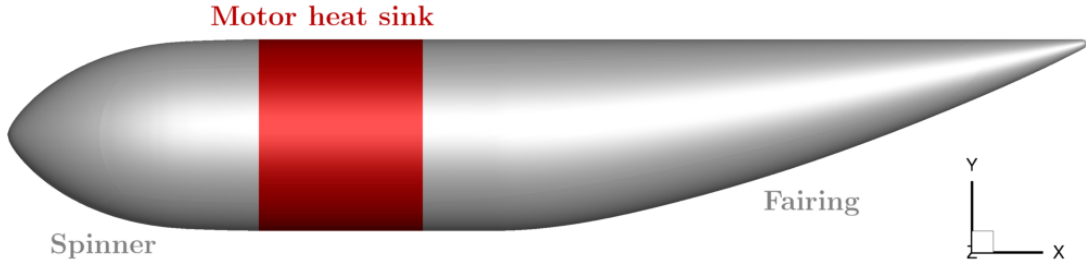


Figure 2: Simplified X-57 high-lift motor nacelle geometry used as the baseline design.

subset of calculations. The MPhys library helped us create our model by providing existing components that wrapped the solvers used in this work (ADflow, TACS, and MeldThermal). Utilizing OpenMDAO facilitated the construction of a flexible model with modular components that can be swapped, such as the heat transfer model. Furthermore, OpenMDAO supplied bindings and implementations of algorithms that were applied at different levels in our model. An optimizer selected from the open-source optimization package pyOptSparse [Wu et al. \(2020\)](#) drives the model by selecting design variables. The design variables selected by the optimizer are passed to the geometry component, which uses pyGeo ¹ to modify the conduction volume mesh and surface mesh of the convection model. The parameterization used in pyGeo is set by the user; details of our parameterization are given in Section 2.7.1. Next, the mesh warping tool IDWarp [Secco et al. \(2021\)](#) modifies the volume meshes used in the aerodynamic and heat transfer analyses according to the deformation of the surface mesh. Then, the heat transfer analysis computes the value of the heat transfer rate. The heat transfer model could either be a convection-only or a conjugate model. Details of the convection and conjugate model can be found in sections 2.4.2 and 2.4.4, respectively. Finally, a separate aerodynamic analysis computes the drag of the design (details given in Section 2.3). The components and the connections between them are shown in Figure 9 as an extended design structure matrix (XDSM) diagram [Lambe and Martins \(2012\)](#).

2.3 Aerodynamic model

The solution of the steady Reynolds-averaged Navier–Stokes (RANS) equations model fluid flow around the nacelle and the drag in the cruise condition. The governing equations incorporate an SA turbulence model to model the turbulent boundary layer. We use the open-source computational fluid dynamics (CFD) solver ADflow ² [Mader et al. \(2020\)](#) to solve the governing equations. In addition to solving the equations, ADflow integrates the forces and provides the aerodynamic coefficients. We selected ADflow because its efficient implementation of the discrete adjoint method makes it ideal for gradient-based optimization [Kenway et al. \(2019\)](#). In addition, ADflow uses an approximate Newton–Krylov (ANK) algorithm, which is fast and robust [Yildirim et al. \(2019\)](#). Despite the ANK algorithm’s robustness, we found that a good initial guess was necessary to avoid stalling the Newton solver in our application. Thus, we

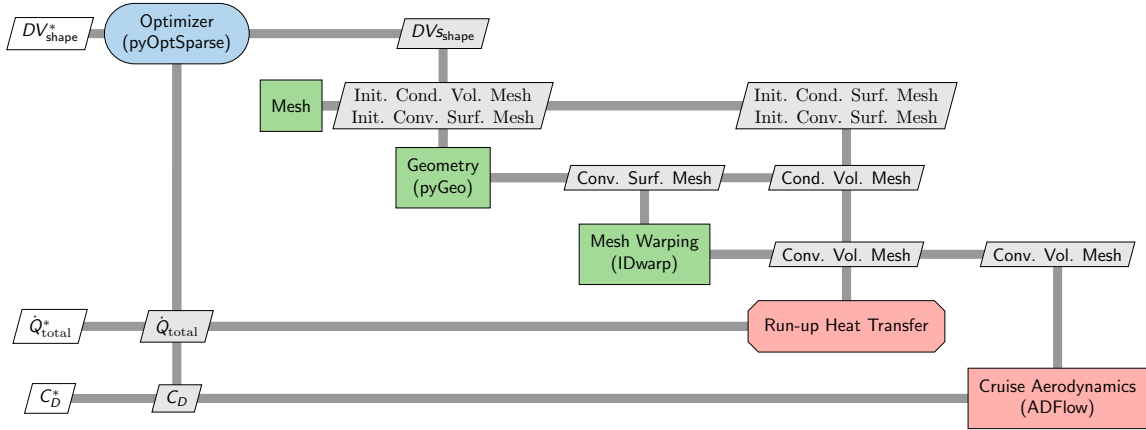


Figure 3: XDSM of the model to analyze and optimize the nacelle heat exchanger.

limit the design variables' rate of change and start each new analysis from the previous analysis to provide a good initial guess.

We used the commercial meshing software ICEM CFD to create a surface mesh of the nacelle from the CAD geometry. This surface mesh was then extruded using the open-source hyperbolic mesh extrusion tool pyHyp³. Figure 4 shows the C_p distribution of the baseline design over the surface of the nacelle as well as the surface mesh (shown in light gray).

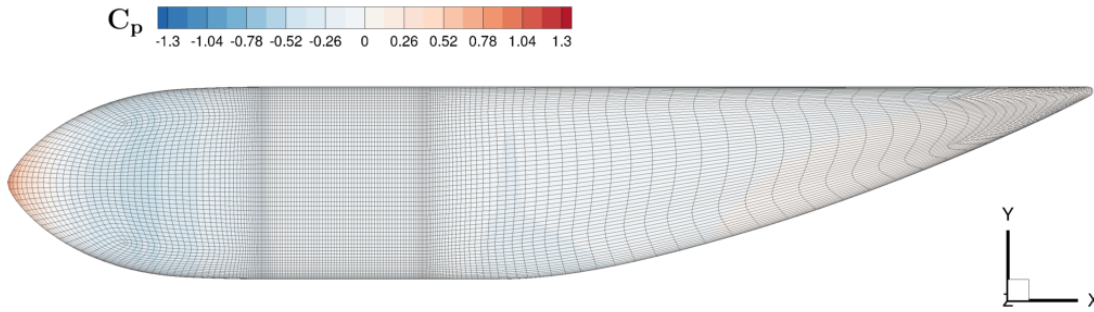


Figure 4: Pressure coefficient distribution on the surface of the baseline nacelle and CFD surface mesh.

2.3.1 Aerodynamic model conditions

The ambient conditions model the atmospheric conditions during the cruise segment of the X-57's design mission. The efficiency of the X-57 is impacted most by the drag at cruise because cruise is the longest mission segment. During cruise, the drag of the twelve cruise motors contributes 9% of the total drag and 22% of the drag from just the wings [Deere et al. \(2017\)](#). [Schnulo et al. \(2019\)](#) detail the mission plan for the cruise segment; during cruise, the X-57 will fly at an altitude of 6000 ft at a speed of

105 kts. The standard atmospheric model at 6000 ft is used to determine the ambient conditions of the atmosphere during cruise. For this segment, we assumed an angle of attack of 4° based on the optimal efficiency trajectory of Falck et al. (2017). We also consider an optimization case where the angle of attack is set to 0° to consider the effect the asymmetric inflow has on the optimized designs.

Because the motor remains powered off during the cruise segment, the heat sink will reduce in temperature until it reaches the ambient air temperature. The boundary conditions of the CFD mesh reflect this; The heat sink was given the same surface temperature as the ambient air. Additionally, the walls of the nacelle were modeled as adiabatic

2.3.2 Aerodynamic CFD mesh convergence study

We performed a mesh size study to verify the accuracy of the mesh selected for optimization. We generated five different mesh sizes; The largest was 5 million cells and each subsequent mesh had about four times fewer cells. The cruise drag value for each mesh was computed. An estimate for the value of an infinitely fine mesh was determined using Richardson extrapolation. Figure 5 shows the results of the converge study along with the Richardson extrapolation point, which served as the reference value for accuracy. We chose the 1 million cell mesh for the aerodynamic analysis since the drag was accurate to 1.5% but was much less costly to solve than the 5 million cell mesh.

2.4 Heat transfer models

Heat moves from the motor coil to the air through conjugate heat transfer. This work uses two different heat transfer models: a simplified convection-only model and a conjugate model. The joule heating in the coils and joule heating in the stator iron due to eddy currents are the primary sources for waste heat production in the motor Deisenroth and Ohadi (2019). The heat from inside the motor is conducted to the outer mold line through the heat exchanger. Convective heat transfer moves the heat from the outer mold line of the heat exchanger into the surrounding air. A schematic view of this process is shown in Figure 6. The heat is transferred from the motor to the air through conduction and convection and thus can be described as conjugate heat transfer. The conditions at the outer mold line couple the conductive and convective heat transfer. In this work, we consider a conjugate model that uses iteration to resolve the coupling between these two models to create the conjugate heat transfer model and a simplified convection-only model that ignores the changes to the surface temperature due to conduction and uses only convection.

2.4.1 Heat transfer modeling conditions

The condition used for the heat transfer model is the preflight motor run-up during a hot day at Edwards Air Force base. During the preflight motor run-up, the plane remains stationary on the runway while all high-lift motors are operated at full throttle to check their function before takeoff. Schnulo et al. (2019) found this condition has

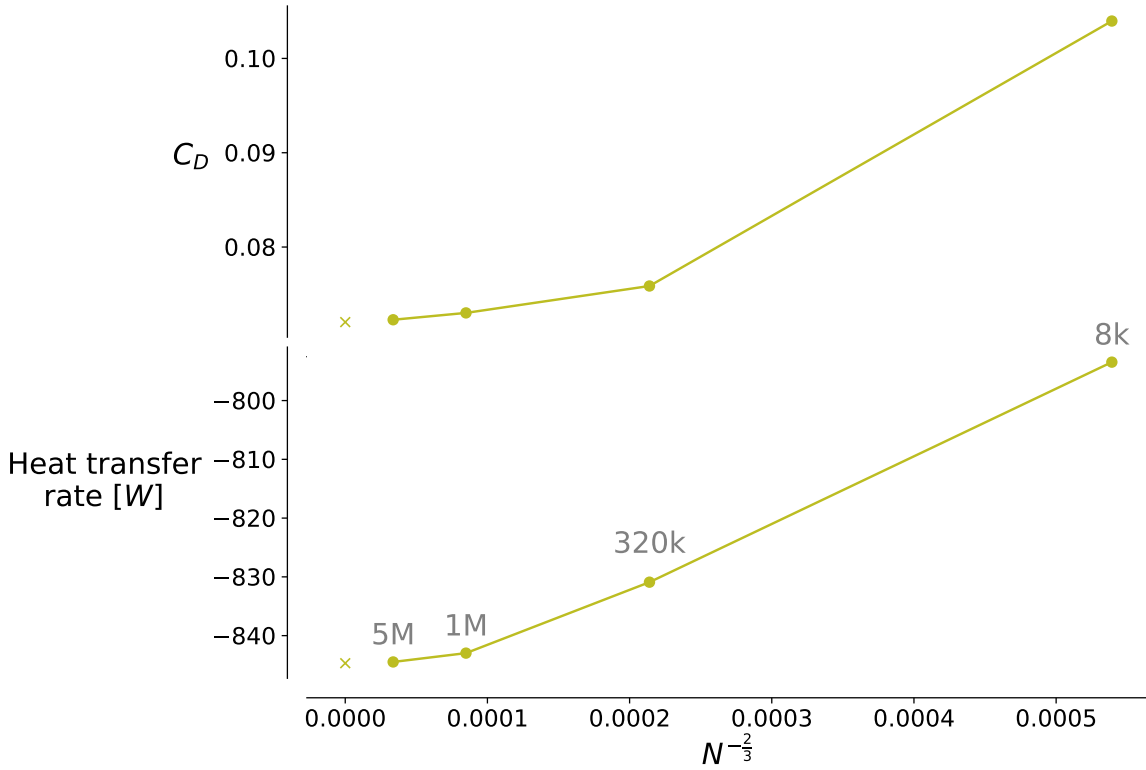


Figure 5: Mesh convergence study, where ‘x’ represents the Richardson extrapolation point and N represents the total number of cells in the volume mesh.

the greatest thermal loads of all mission segments. In the analysis of the preflight run-up condition, [Schnulo et al. \(2019\)](#) approximated the influence of the propeller by removing the rotating propellers and adding a uniform stream speed of 32 m/s. We adopt this same simplification to make the modeling tractable for optimization. The impact of removing the swirl of the propeller slipstream from the model is discussed in Section 3. If it is already hot outside, the smaller temperature difference between the heat exchanger and the air will slow the rejection of waste heat. Thus, the thermal management of the X-57 has its worst-case loading on the hottest possible testing day. At Edwards Air Force base, where the aircraft will be tested, this worst-case ambient temperature is 45 °C; an additional margin of 15 °C for safety is added for a maximum ambient temperature of 60 °C [Hall et al. \(2019\)](#).

Note that the conditions used to evaluate the heat sink’s heat rejection capability and drag are different. Although drag can be non-dimensionalised by flow speed, the heated boundary condition and angle of attack result in different non-dimensionalised drag values. In the baseline design, the computed drag coefficient during the cruise conditions was 16% lower than during the preflight motor run-up condition.

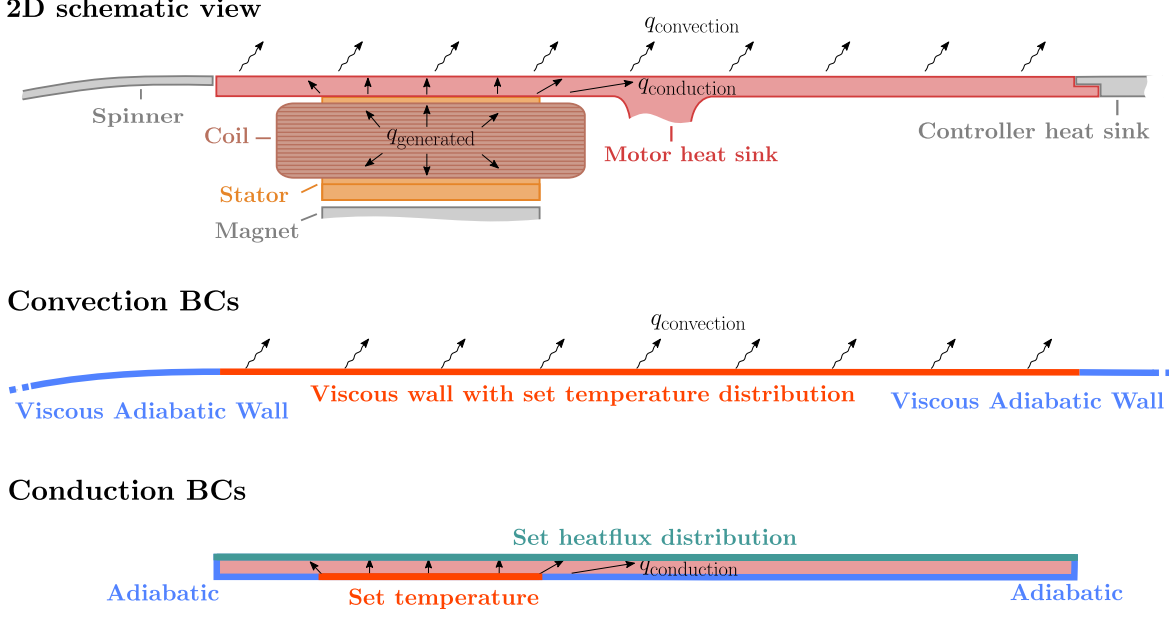


Figure 6: The heat generated in the motor coil is conducted to the motor heat sink and convected to the air. The red motor heat sink is a slice of the heat exchanger shown in Figure 2.

2.4.2 Convective heat transfer

The convective analysis solves the same governing equations from the aerodynamic analysis (RANS with an SA turbulence model). However, the heat exchanger surface uses a temperature distribution boundary condition. The initial surface temperature distribution is set to satisfy the conjugate heat transfer problem of the baseline design. In the conjugate model, the analysis updates this temperature distribution to satisfy the subsequent conjugate heat transfer problems of candidate designs. In the convection-only model, the surface temperature distribution remains the same as the baseline design for each candidate design. We also use ADflow to solve the governing equations for this set of boundary conditions. By reducing all the residuals to zero, the solver determines the flow field and the heat flux distribution on the heat exchanger surface. To compute the total heat transfer rate, ADflow integrates the heat flux over the surface of the nacelle.

We found an upwind flux scheme to be more accurate than the default Jameson–Schmidt–Turkel (JST) scheme when computing the inviscid fluxes for this application. The JST scheme in ADflow uses an entropy sensor to determine where to add artificial dissipation. At the junction of the adiabatic wall and the heated surfaces of the nacelle, there is a sharp change in the entropy. This leads JST to add dissipation to these regions, distorting the heat flux at the beginning and end of the heat exchanger. Figure 7 shows the temperature field used for the temperature distribution boundary condition and resulting surface heat flux of the baseline design with the surface mesh in light grey. The heat flux at the forward portion of the heat exchanger is the greatest as the thermal boundary layer is first established there, and the temperature gradient in the off-wall direction is the largest. Aft of the heat sink, the wall is adiabatic and

thus must match the hot air temperature convected downstream.

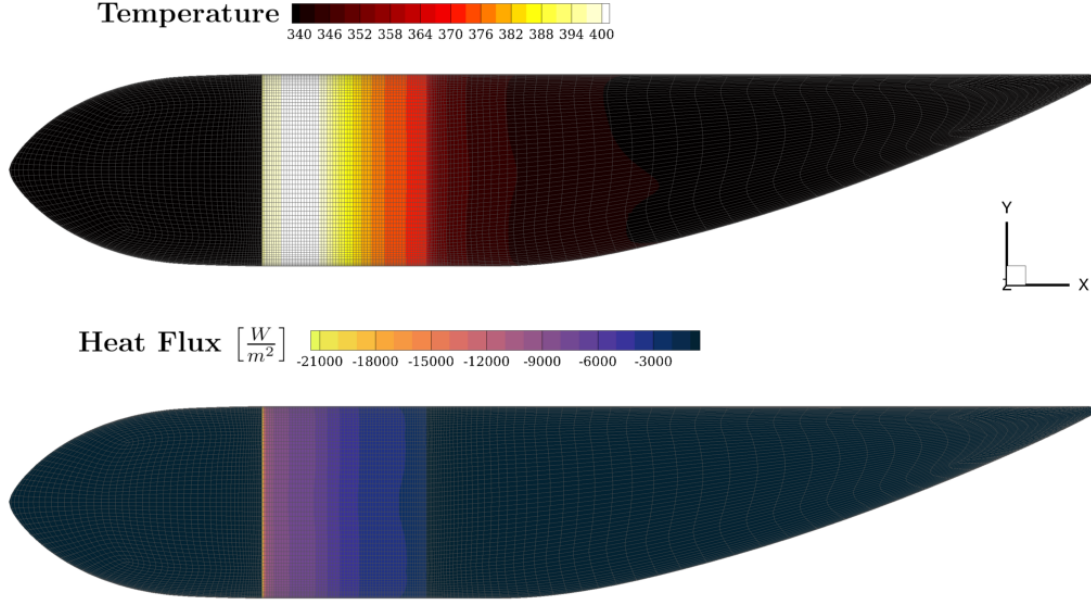


Figure 7: Convective heat transfer analysis of the baseline configuration. The heat sink has a set temperature distribution boundary condition, while the unheated walls have an adiabatic boundary condition.

To validate our convection model, we compared its results to those of an experiment. Schnulo et al. (2019) conducted wind tunnel experiments to determine the heat transfer rate of the high-lift motor heat exchanger as a function of wind speed. The temperature distribution used in our validation analysis was set to match the temperature distribution of the computational simulation at 32 m/s by Schnulo et al. (2019). The average heat transfer rate was computed by taking the area-weighted average of each cell’s local heat transfer coefficient on the surface mesh. The value of the average heat transfer coefficient from our CFD model is compared with the experimental value from 20 to 70 m/s in Figure 8. At the freestream speed used in our convection analysis, 32 m/s, our model had a relative error of 2.1%. The difference between our CFD model and experimental data increases as the speed increase and reaches a relative error of 7.5% at 70 m/s.

One explanation for the increase in relative error with speed is the change in the surface temperature distribution of the experimental model due to higher convective heat flux. It would be beneficial to have the experimental temperature distribution at each data point to improve the validation. However, because the model is accurate at our design point, further improvements to our validation study were left for potential future work.

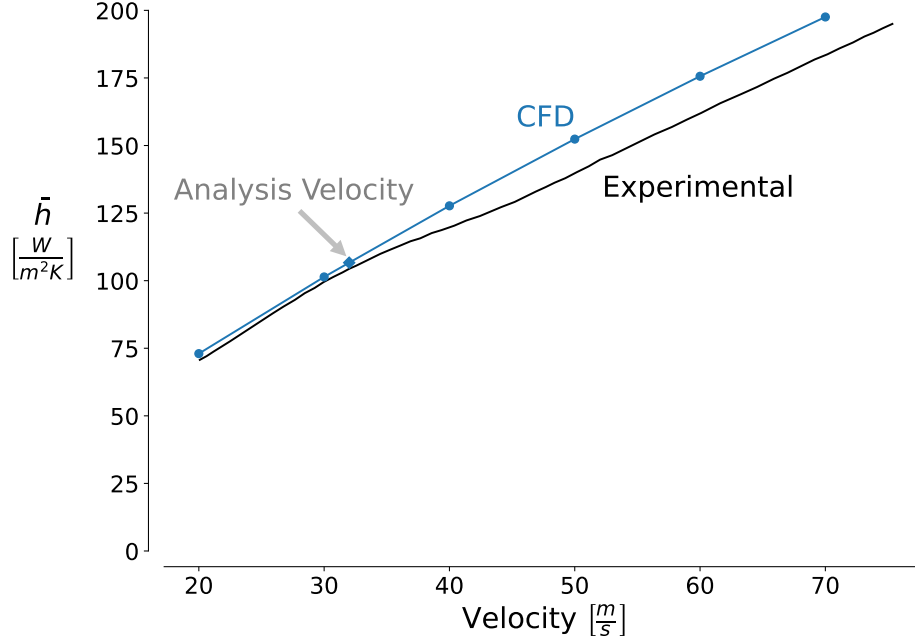


Figure 8: The convection model differs from the experimental value by 2.1% at the design point.

2.4.3 Convective CFD mesh convergence study

Similar to the aerodynamic mesh convergence study in Section 2.3.2, we perform another mesh convergence study using the same set of meshes to verify the accuracy of the mesh for the convective analysis. For this study, we used a uniform surface temperature of 400° Kelvin. The results of this study are shown in Figure 5 alongside the results of the aerodynamic mesh convergence study. We also selected the 1 million cell mesh for the convective analysis since the heat transfer rate value was only 0.2% different than the Richardson extrapolation value but was much less costly to solve than the 5 million cell mesh.

2.4.4 Conjugate heat transfer model

We apply a partitioned solvers approach to model the conjugate heat transfer from the motor. We use separate solvers for the convective and conductive heat transfer models instead of a monolithic approach where both sets of equations are solved simultaneously. The work of Verstraete (2016) describes the coupling approaches that can be used for partitioned solvers in conjugate heat transfer problems. We use the flux forward, temperature back (FFTB) approach, which follows the convention of Divo et al. (2003) to name the method based on the qualities passed from and into the fluid domain solver. For a given surface temperature, T_{conv} , the convective analysis computes the resulting heat flux, \dot{q}_{conv} . The transfer scheme then converts the heat flux from the convective mesh, \dot{q}_{conv} , to the conduction mesh, \dot{q}_{cond} . Given a heat flux vector, \dot{q}_{cond} , the conduction analysis computes the surface temperature distribution, T_{cond} . The transfer scheme transfers the surface temperatures from the conduction

analysis, T_{cond} , to surface temperatures for the convection analysis, T_{conv} . We ensure that the energy exiting the solid domain and entering the fluid domain is the same by iterating through the model until the heat fluxes have converged. Figure 9 illustrates the coupling between the convection and conduction models. By connecting the coupling variables of the components and applying the nonlinear block Gauss–Seidel algorithm to solve the system, we implemented the conjugate model with an FFTB approach in OpenMDAO. It is possible that a heat transfer coefficient forward and temperature back approach would have been faster to solve, but the mixed, or Robin, boundary conditions needed for the heat transfer coefficient boundary condition would have required additional implementation effort to use in our conductive analysis.

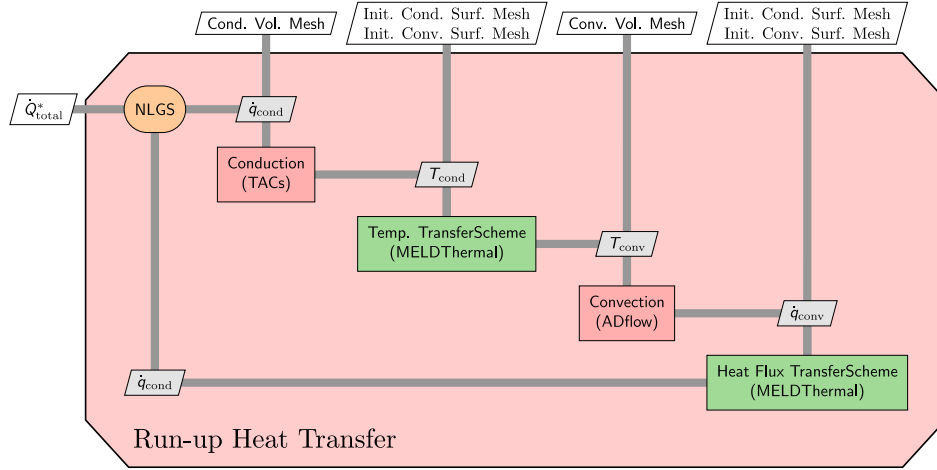


Figure 9: The XDSM of the conjugate heat transfer model shows the coupling variables and the solvers used inside the model.

The Biot number is the ratio of conductive thermal resistance to convective resistance.

$$Bi = \frac{hL}{\kappa} \quad (1)$$

Verstraete and Scholl (2016) have shown that the FFTB approach is unstable for problems with a Biot number greater than one. Under-relaxation can stabilize the scheme if the Biot number is greater than one, although it was not needed in this case. In our case, an order of magnitude analysis confirms that the Biot number of our problem is less than one for all candidate designs. The convective heat transfer coefficient, h , is on the order of 100, and the conductivity, κ , of the heat sink is on the order of 100 as well. The characteristic length of the heat sink, L , is the local thickness, which is on the order of millimeters to 10s of millimeters. Thus, the resulting local Biot numbers are less than 0.1 because of the small characteristic lengths of the heat exchanger.

2.4.5 Conductive heat transfer

We model the conductive heat transfer using a finite element model with a temperature boundary condition for the motor and a heat flux boundary condition for

the outer mold line. The steady-state heat conduction equation with non-temperature dependent conduction is the governing equation for this model.

$$\mathbf{q} = -k\nabla T \quad (2)$$

In this work, we limit the conduction domain to a simplified version of the heat exchanger itself. The air gap between the spinner and heat exchanger prevents heat from conducting forward. The heat exchanger is connected via screws to another heat exchanger for the motor controller aft of the heat exchanger. We assume that the heat exchanger does not transfer any heat to the motor controller heat exchanger to simplify our model. The motor controller heat exchanger is also heated, and modeling the heat transfer between the two would require modeling the additional heat sources. Furthermore, we would expect this heat transfer to be small because the two heat exchangers are connected with tabs that have a small contact area. The extra material of the heat exchanger used to hold the motor axial and the tabs used to connect to the motor controller heat exchanger are also ignored. Instead, the heat exchanger is modeled as a uniformly thick annulus of 4 mm for the baseline design.

To solve the heat conduction problem on the simplified domain, we used the open-source finite element toolkit TACS [Kennedy and Martins \(2014\)](#). TACS was selected over other finite element toolkits because of its highly scalable algorithms and efficient implementation of the adjoint method for finding sensitivities. The solution for the baseline problem using TACS is shown in Figure 10. The boundary conditions (BCs) model the contact between the motor and heat sink as well as the air flowing along the upper surface and are shown in Figure 6. The outer side of the heat exchanger is set using a Neumann BC to specify the heat flux acting at each node due to the convective heat transfer. The front and back sides of the heat exchanger are also set using a Neumann BC but are set as adiabatic (zero heat flux). On the inner side of the heat sink, the nodes in contact with the motor’s stator teeth are set to the maximum allowable temperature of the motor (Dirichlet BC) and the remainder are set as adiabatic. The heat load of the motor could also be applied as a heat flux boundary condition, but another boundary condition would need to change to avoid the ambiguity from all Neumann boundary conditions. The material properties used for the heat exchanger come from [Hall et al. \(2019\)](#), who modeled the heat exchanger as a solid piece of 2024-T3 aluminum with a thermal conductivity of 120 W/m·K.

2.4.6 Transfer scheme

We use MeldThermal [Kiviaho and Kennedy \(2019\)](#); [Smith et al. \(2021\)](#) from the open-source software FUNtoFEM to transfer the temperatures and heat fluxes between the convection and the conduction meshes. The scheme uses an inverse distance approach to weigh the contributions of N nearest neighbors when interpolating data between the meshes. We chose to create conduction and convection meshes that were approximately coincident. The error due to interpolation when transferring between meshes is limited with these meshes. Reducing the interpolation error led to analysis results that preserved local features better and improved optimization results.

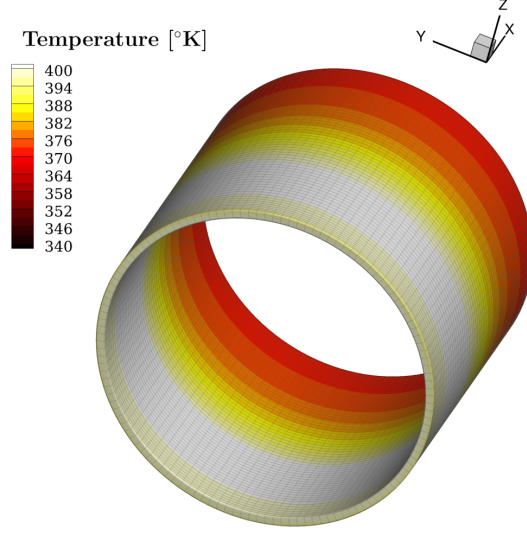


Figure 10: Temperature distribution of the heat sink in the baseline design. TACS is used to solve the heat conduction equation to find the temperature distribution.

2.5 Model derivatives

We compute component derivatives using a combination of reverse mode algorithmic differentiation (AD) and the adjoint method. OpenMDAO combines the component derivatives using the unified derivatives equation (UDE) to form total derivatives [Martins and Hwang \(2013\)](#); [Hwang and Martins \(2018\)](#). The UDE forms the backbone of OpenMDAO [Gray et al. \(2019\)](#), which focuses on gradient-based optimization. The UDE can be thought of as a generalization of the chain rule and is implemented in OpenMDAO to combine the derivatives of both explicit and implicit components effectively.

To illustrate how the derivatives are combined within our model in OpenMDAO, we consider the derivatives of our objective function, which is the drag coefficient, C_D . The optimizer requires the total derivatives of the functions of interest with respect to all the design variables to optimize the design. These total derivatives can be formed by combining the total derivatives of the sub-components that make up the model. For the case where C_D is the function of interest, the combination of component derivatives is written as

$$\frac{dC_D}{dx} = \underbrace{\frac{dC_D}{dX_v}}_{\text{ADflow IDWarp}} \underbrace{\frac{dX_v}{dX_s}}_{\text{pyGeo}} \underbrace{\frac{dX_s}{dx}}_{\text{pyGeo}}. \quad (3)$$

The derivatives of the explicit components (geometry, mesh warping, and transfer schemes) are computed using algorithmic differentiation (AD). The geometry component is only a function of the design variables, x , and thus $dX_s/dx = \partial X_s/\partial x$. Similarly, The mesh warping component is only a function of surface node coordinates, X_s , and thus $dX_v/dX_s = \partial X_v/\partial X_s$. The derivatives of the implicit components (aerodynamic, conduction, and convection), on the other hand, require an analytic approach

to solve efficiently since the variables lack an explicit relationship. For the aerodynamic model, the total derivatives of C_D with respect to the mesh points is written as

$$\frac{dC_D}{dX_v} = \frac{\partial C_D}{\partial X_v} + \frac{\partial C_D}{\partial u} \frac{du}{dX_v} \quad (4)$$

The first term on the right-hand side (RHS) reflects the explicit dependence of C_D on the volume mesh node positions, X_v . The second term reflects how the coefficient of drag is implicitly dependent on nodal positions of the volume mesh through the states of the flow field, u . This dependence is a result of the solver, which modifies the states of the flow field until the total residual is zero (or as near as we can get), for a given set of nodal positions. Because the solver modifies the states such that $r = 0$ for any set of node positions, $dr/dX_v = 0$ as well. This second condition dictates the relationship between the components of the residual total derivative.

$$\begin{aligned} \frac{dr}{dX_v} = 0 &= \frac{\partial r}{\partial X_v} + \frac{\partial r}{\partial u} \frac{du}{dX_v} \\ -\frac{\partial r}{\partial X_v} &= \frac{\partial r}{\partial u} \frac{du}{dX_v} \\ -\frac{\partial r^{-1}}{\partial u} \frac{\partial r}{\partial X_v} &= \frac{du}{dX_v} \end{aligned}$$

This relationship can be substituted back into the equation for the total derivative of C_D to define the total derivative using only partial derivatives.

$$\frac{dC_D}{dX_v} = \frac{\partial C_D}{\partial X_v} - \frac{\partial C_D}{\partial u} \frac{\partial r^{-1}}{\partial u} \frac{\partial r}{\partial X_v} \quad (5)$$

Evaluating equation 5 requires solving a linear system. One can choose to either solve

$$-\frac{\partial r^{-1}}{\partial u} \frac{\partial r}{\partial x}$$

or

$$\underbrace{-\frac{\partial C_D}{\partial u} \frac{\partial r^{-1}}{\partial u}}_{\psi^T}$$

. Solving the first one results in the direct method, while using the second option results in the adjoint method. Using the adjoint method is more efficient when there are more design variables than functions of interest. In our case, we only have two functions of interest computed with the implicit models; therefore, we use the adjoint method.

One can reduce the implementation effort for the adjoint solver by reusing some routines of the primal solver. To compute the partial derivatives in equation 5 we use reverse and forward mode AD similar to the rest of ADflow. [Kenway et al. \(2019\)](#) provide an extensive overview of the AD approach of ADflow and the implementation used to compute the total derivatives efficiently. The primal solver of ADflow uses a

Newton–Krylov method in the final stages of convergence. The Jacobian in the adjoint method is the transposed version of the final Jacobian used in the Newton–Krylov method and consequently shares the same family of eigenvalues. Both linear systems are solved using a Krylov subspace method. In practice, mirroring the method used to solve the primal equations has the added benefit of assuring convergence of the adjoint system.

2.5.1 Coupled derivative computation

For the conjugate heat transfer model, the coupled sensitivities are solved with the coupled adjoint method using linear block Gauss–Seidel. For the heat transfer model, the function of interest is the value of the heat transfer constraint, \dot{Q}_{total} . The state variables of the conjugate heat transfer model are simply the concatenation of the flow state variables of the convection model, u_{conv} , and the temperature state variables of the conduction model, u_{cond} .

$$u_{\text{conj}} = \begin{bmatrix} u_{\text{conv}} \\ u_{\text{cond}} \end{bmatrix}$$

Likewise, the residuals of the conjugate model are formed by concatenating the residuals of the convection and conduction models.

$$r_{\text{conj}} = \begin{bmatrix} r_{\text{conv}} \\ r_{\text{cond}} \end{bmatrix}$$

Consequently, the adjoint system of the conjugate model can be written using some terms of the components of the adjoint systems of the convection and conduction models. The block diagonal terms of the Jacobian are the Jacobians of the convection and conduction models. While the off-diagonal blocks, $\partial r_{\text{conv}}/\partial u_{\text{cond}}$ and $\partial r_{\text{cond}}/\partial u_{\text{conv}}$, represent the derivatives of the coupling between the convection and conduction models.

$$\begin{bmatrix} \frac{\partial r_{\text{conv}}}{\partial u_{\text{conv}}} & \frac{\partial r_{\text{conv}}}{\partial u_{\text{cond}}} \\ \frac{\partial r_{\text{cond}}}{\partial u_{\text{conv}}} & \frac{\partial r_{\text{cond}}}{\partial u_{\text{cond}}} \end{bmatrix}^T \begin{bmatrix} \psi_{\text{conv}} \\ \psi_{\text{cond}} \end{bmatrix} = - \begin{bmatrix} \frac{\partial \dot{Q}_{\text{total}}}{\partial u_{\text{conv}}} \\ \frac{\partial \dot{Q}_{\text{total}}}{\partial u_{\text{cond}}} \end{bmatrix}$$

To solve the adjoint system of the conjugate heat transfer problem, we use an iterative blocked approach. If we know ψ_{cond} then we can use the convection-specific adjoint solver, but with an augmented RHS, to determine the value of ψ_{conv} using

$$\frac{\partial r_{\text{conv}}}{\partial u_{\text{conv}}}^T \psi_{\text{conv}} = -\frac{\partial \dot{Q}_{\text{total}}}{\partial u_{\text{conv}}} - \frac{\partial r_{\text{cond}}}{\partial u_{\text{cond}}}^T \psi_{\text{cond}}$$

Similarly, If we know ψ_{conv} then we could use the conduction-specific adjoint solver, but with an augmented RHS, to determine the value of ψ_{cond} .

$$\frac{\partial r_{\text{cond}}}{\partial u_{\text{cond}}}^T \psi_{\text{cond}} = -\frac{\partial \dot{Q}_{\text{total}}}{\partial u_{\text{cond}}} - \frac{\partial r_{\text{conv}}}{\partial u_{\text{conv}}}^T \psi_{\text{conv}}$$

Using these two equations in an iterative loop with an initial estimate of ψ_{cond} and ψ_{conv} is the basis of the coupled adjoint method. This method is has been utilized

previously for aerostructural problems [Martins et al. \(2005\)](#) and conjugate heat transfer problems [Burghardt et al. \(2020\)](#). During each iteration, using the solution of ψ from the first equation in the second leads to the Gauss–Seidel method. OpenMDAO has an implementation of this algorithm, linear block Gauss–Seidel, which uses the adjoint solvers of each component and the reverse mode routines. Once the algorithm converges, the total sensitivity is then assembled by OpenMDAO using

$$\frac{d\dot{Q}_{\text{total}}}{dX_v} = \frac{\partial\dot{Q}_{\text{total}}}{\partial X_v} + \psi_{\text{conv}}^\top \frac{\partial r_{\text{conv}}}{\partial X_v} + \psi_{\text{cond}}^\top \frac{\partial r_{\text{cond}}}{\partial X_v}.$$

2.6 Derivative verification

We used the complex-step method [Martins et al. \(2003\)](#) to verify the accuracy of the derivatives for each component and subsequently the whole model. This method provides a more accurate derivative approximation than the finite-difference method ([Martins and Ning, 2022](#), Ch. 6). The accuracy of the finite difference method is limited by the loss of significant digits in the result due to the small differences between the unperturbed and perturbed states. Tables 1 and 2 show the results of the complex step verification of the whole model using a coarse CFD mesh.

As is often the case in practice, we do not match the value of the complex step to the full 16 digits. We suspect this discrepancy is caused by the limited accuracy of the primal solution itself. The accuracy of dr/du is limited by the accuracy of the primal residuals, which lack 16 digits of significance due to the truncation error in the flux functions and flux summation. In practice, it is observed that the final derivatives are only accurate to an error of about 10^{-13} relative to the initial residual.

dC_D/dx			
FD	−0.1496893167495728	0.0633765459060669	0.072439968585968
CS	−0.1496679623088565	0.0633866010196038	0.072467500456739
AD	−0.1496679623088468	0.0633866010195695	0.072467500456696
$\frac{ CS-AD }{CS}$	$6.49066862 \times 10^{-14}$	$5.41216770 \times 10^{-13}$	$6.00172308 \times 10^{-13}$

Table 1: The analytic and complex step derivatives of the objective function match to the expected level of accuracy.

$d\dot{Q}_{\text{total}}/dx$			
FD	−53.97048950195313	−60.5118408203125	−60.229568481445
CS	−53.97018831488005	−60.51184881889078	−60.229389563990
AD	−53.97018831486155	−60.51184881892896	−60.229389564058
$\frac{ CS-AD }{CS}$	$3.42697107 \times 10^{-13}$	$−6.31026276 \times 10^{-13}$	$−1.12298271 \times 10^{-12}$

Table 2: The analytic and complex step derivatives of the conjugate heat transfer constraint match to the expected level of accuracy.

2.7 Optimization problem

The objective of the optimization is to minimize the nacelle drag coefficient by varying the nacelle shape subject to transfer heat and thickness constraints. Section 2.7.1 describes how the design variables are used to adjust the nacelle shape. Furthermore, Section 2.7.2 describes the constraints and how we selected the values for the constraints. Table 3 provides a summary of the optimization problem.

Table 3: Nacelle heat exchanger optimization problem

	Variable	description	Quantity
minimize	C_D	Drag coefficient of the nacelle	1
with respect to	r	Radial coordinate of the FFD control points	48
subject to	$\dot{Q} \geq \dot{Q}_{\max}$	Total heat transfer rate during run-up condition is greater than waste heat production	1
	$t \geq \frac{1}{2}t_0$	The thickness is greater than or equal to half the original thickness	756

2.7.1 Design variables

The design variables alter the shape of the outer mold line of the heat exchanger. This is accomplished using pyGeo’s implementation of the free form deformation (FFD) technique [Sederberg and Parry \(1986\)](#). The technique works by first using a set of control points to define a splined volume. To initialize the geometry manipulation, the nodes of the baseline geometry are located within the volume in terms of the parametric coordinates of the initial splined volume. Changing the position of the control points changes the splined volume and thus the absolute location of the parametric coordinates within the volume. The deformed surface coordinates are computed by evaluating the same parametric coordinates in the new splined volume.

To define annular shape variables, the FFD splined box volume is folded into a ring with an overlap of two control points on each side. The FFD control points beyond the overlap are moved the same amount as the coincident nodes to ensure the volume at the overlap is deformed correctly. The entire conduction volume mesh is embedded and modified by the control points. Only the convection surface mesh is embedded into the volume because the mesh warping algorithm (IDWarp) propagates the deformations into the volume mesh efficiently while still ensuring a high-quality mesh. Figure 11 shows the baseline design and control points and examples of how the design can be modified by the control points.

The selection of 16 circumferential FFD points implicitly limits the design to a maximum of 8 circumferential fins. Increasing the circumferential refinement of the FFD would increase the size of the design space but would allow thin features that cannot be adequately resolved on the CFD surface mesh. Refinement of the CFD surface would provide improved resolution for thin features but would make the analysis and optimization much more difficult to solve. To parameterize a design that could change from zero fins to over 100 (like the one shown in Figure 1a) the surface mesh

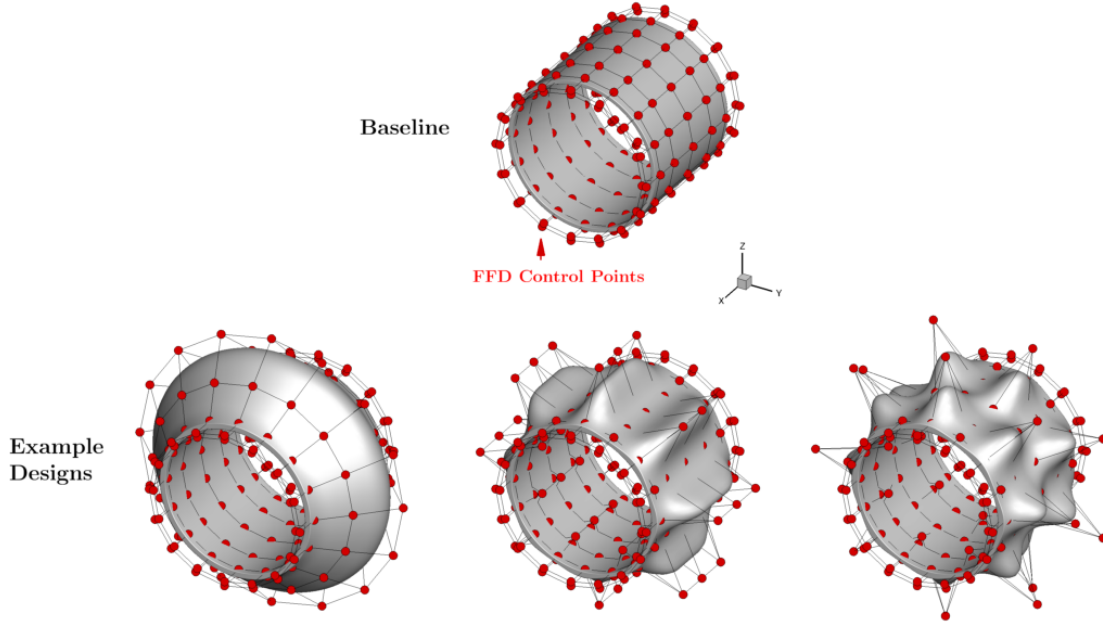


Figure 11: The baseline geometry and control points (top) and three example deformations (bottom) demonstrating shapes that can be produced by the design variables.

would have to be uniformly refined four times. The resulting volume mesh would have approximately 320 million cells, making it extremely challenging to analyze and practically impossible to use for optimization.

We view the challenge of parameterizing and analyzing thin features as critical to heat exchanger shape optimization. However, this challenge is most critical when the required heat rejection is much greater than that of a smooth surface only and thus requires a significant surface area increase. Because our maximum required heat load is only 50% greater than what can be generated by a smooth surface alone (as described in Section 2.7.2), we expect this challenge to have a reduced impact on our results. To partially examine the impact this limitation has on our results, we compare a design with 16 fins and a design with 8 fins to the optimized designs in Section 3.2.

2.7.2 Constraints

The constraints ensure that the heat sink maintains a minimum thickness of 2 mm and that the heat sink can reject the required heat loads. The thickness is measured from the inner surface to the outer surface at 756 uniformly spaced positions on the heat exchanger. To ensure the optimized designs can be manufactured, the thickness of the heat sink was limited to a minimum of 2 mm to prevent unrealistically thin geometries. As highlighted in the introduction, even though electric motors have a high efficiency, they produce considerable waste heat. Each of the X-57's high-lift motors is designed to produce 13.7 KW of power with an efficiency of 96.6% [Hall et al. \(2019\)](#). We assume about 80% of the waste heat is generated in the coils and stators based on the work

of Deisenroth and Ohadi (2019). As a result, the baseline constraint is approximately 400 W. Dubois et al. (2016) showed a trade-off in the efficiency and mass of electric motors designed for distributed electrical propulsion. For the set of Pareto optimal designs of Dubois et al. (2016), the motor’s weight ranged from 10 to 30 kg, and the efficiency ranged from 94 to 97%. To examine the consequence of swapping the high-lift motor with lighter but less efficient ones, we enforce constraint values from 400 W up to 600 W in 50 W steps. The constraint value of 600 W corresponds to a motor efficiency of approximately 94.5%. Changing the weight of the motor and heat sink will have additional aircraft-level performance effects. However, for this component-level study, we do not consider these effects since it is outside of our scope.

2.7.3 Optimizer

We selected the Sparse Nonlinear Optimizer (SNOPT) Gill et al. (2002) to solve the optimization problem because it efficiently handles expensive function evaluations using its gradient-based algorithm. The CFD evaluations required for the aerodynamic and heat transfer models make the objective and constraints expensive to evaluate. To keep the cost of the optimization tractable, gradient-based optimization must be used with analytical methods for computing the gradients. SNOPT has been utilized effectively in prior aerodynamic shape optimization work Yu et al. (2018).

We applied scaling to improve the conditioning of the optimization problem by making all the design variables, objective functions, and constraints of order one. The optimizer was run until it could not decrease the optimality further and exited. We chose not to explicitly set an optimality tolerance to see how low the optimality could be converged for a problem with coupled derivatives. The final optimality the optimizer was able to reach was on the order of 10^{-6} , which corresponds to a relative convergence of approximately 4 or 5 orders of magnitude. The feasibility limit for the problem was set to 10^{-4} for all cases. However, the feasibility was driven down much lower than the tolerance as the optimizer worked to decrease the Lagrangian (the final feasibility for each problem was around 10^{-10}). Plots of optimality and feasibility for each case are shown in Figure 12.

3 Results

This section describes the results of solving the optimization problem described in Section 2.7 using the analysis models described in Section 2.2. The results include the optimization cases with a conjugate heat transfer model and heat transfer constraint values of 400, 450, 500, 550, and 600 W. The values for this constraint were chosen to reflect an increase in the heat load due to a less efficient motor and are explained further in Section 2.7.2. An additional optimization case (described in Section 3.1.1) with a 600 W heat transfer constraint and a 0° angle of attack cruise analysis was started from the optimum of the 600 W case. We also ran optimization cases with a convection-only heat transfer model with heat transfer constraint values of 400, 450, 500, 550, and 600 W. Furthermore, we analyzed all the convection-only optimizations with a conjugate heat transfer model to measure their actual performance. Finally, we

created and analyzed designs with 8 and 16 simple fins sized for 600 W and compared their performance with the optimized design. All cases were converged by the optimizer to the required feasibility and low optimality ($\approx 1 \times 10^{-5}$) as shown in Figure 12

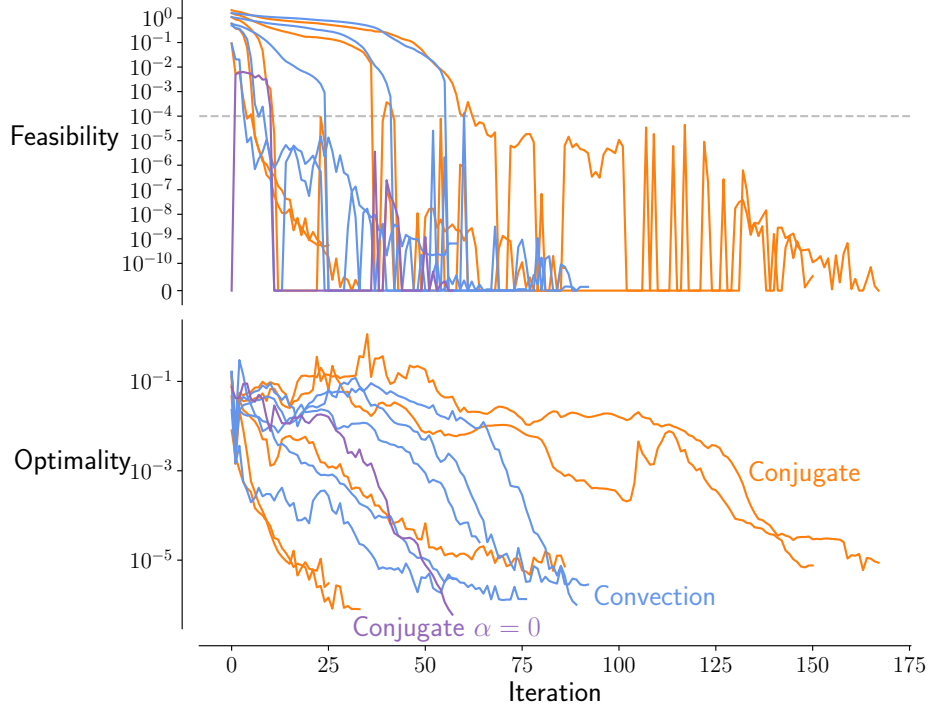


Figure 12: For all problems, the optimizer drove the feasibility below the tolerance of 10^{-4} and the optimality down by about four to five orders of magnitude relative to the initial design.

The optimization results show that the optimal shape changes as the heat transfer value increases. They also show that the convection-only optimizations produced designs with more drag and weight for the same heat transfer constraint value. The optimized shapes develop a top-bottom asymmetry to reduce separation due to the nonzero angle of attack in the aerodynamic analysis more effectively. Furthermore, compared with the simply designed cases with 8 and 16 fins, the optimized shapes have fins that are tilted forward to reduce separation.

3.1 Impact of thermal constraint on the optimal design

As the heat transfer required from the heat exchanger increases, the heat exchanger grows and changes shape. The heat transfer rate, drag values, and mass are shown along with a 2D slice through the center of each heat sink in Figure 13. The 2D slices highlight the key shape differences between the optimized designs, but the heat sinks have streamwise variation as well.

The optimization results using the conjugate heat transfer model develop fins as the required heat load rises. The design optimized to reject 400 W is nearly indistinguishable from the baseline. The optimizer slightly increased the thickness to improve

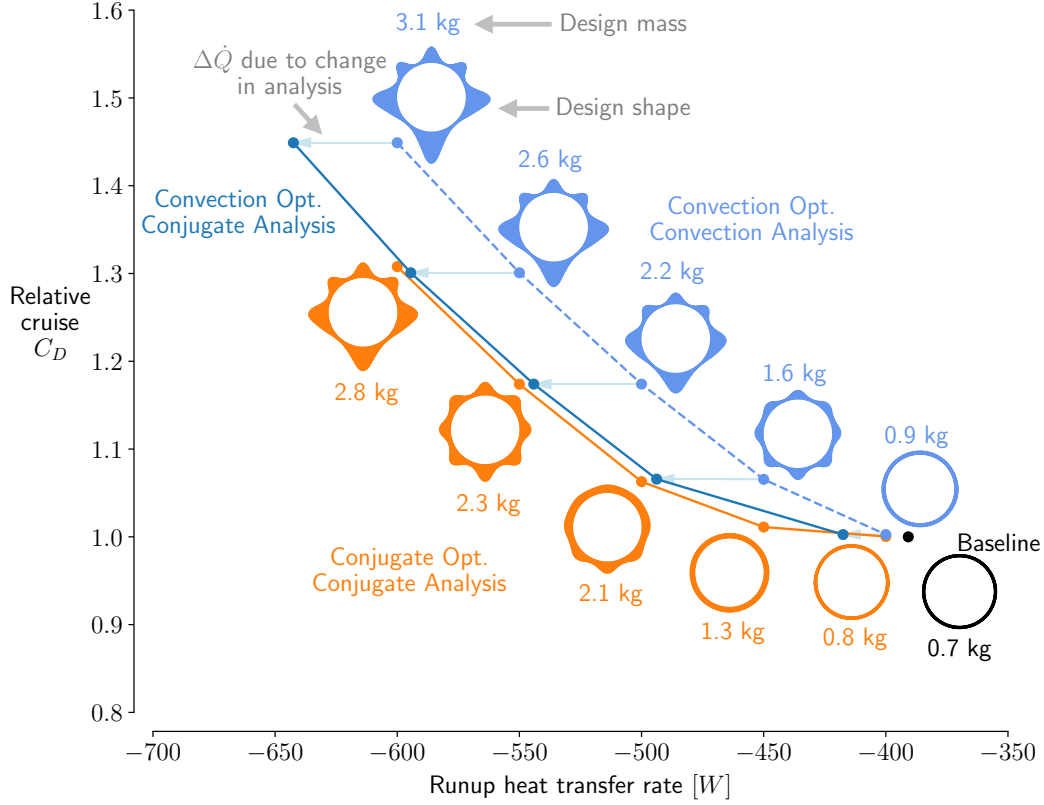


Figure 13: Pareto front of heat transfer versus drag coefficient for both the conjugate and convection models. The dashed blue line shows the computed drag and heat transfer of designs optimized with a convection-only model assessed with a convection-only model. The dark blue line shows the drag and heat transfer of designs optimized with a convection-only model but assessed with a conjugate model. The light blue arrows link the same design assessed with each method and show the change in heat transfer rate due to the change in analysis. The convective designs are heavier for the same specified heat load.

the heat transfer of the baseline from 391 to 400 W. The optimizer expanded the thickness of the heat exchanger even further to accommodate the increase to 450 W. At 500 W, the heat exchanger again increases in thickness, but three small fins form on the bottom surface. When the heat rejection constraint increases even further to 550 W, the surface grows fins along the entire circumference. At 600 W, the bottommost fins merge into three larger fins.

As the heat transfer constraint increases, the optimal designs produce more drag. The designs optimized for 400 and 450 W have about the same drag as the baseline. However, the drag goes up considerably when fins are added to meet the heat transfer constraint value. The fins add a region of high heat transfer and high pressure to the front of the heat sink. The high pressure on the front must be matched on the back to reduce the pressure drag. The fins develop a forward tilt to reduce flow separation and thus reduce the pressure drag at higher heat transfer values.

Figure 14 shows the heat transfer coefficient and pressure coefficient fields over the surface of the optimized nacelle shapes. This figure also shows a side view of

the streamlines passing over the heat sink, with areas where separation is detected highlighted in red. Kenway and Martins (2017) detail the method used to detect separation.

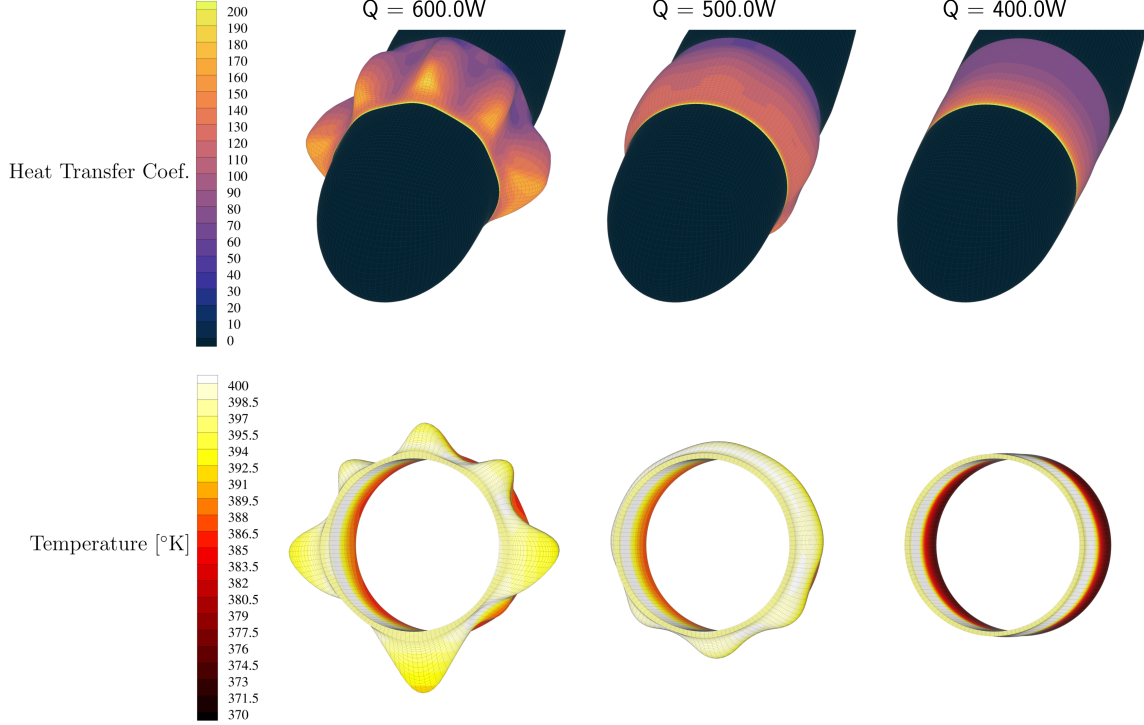


Figure 14: Fins add a region of high heat flux and high pressure on their front side. However, fins also add a region of separation on their aft side when they become large.

The optimization results with the convection-only heat transfer model (shown with the dashed blue line in Figure 13) under-predict the value of the heat transfer and, consequently, produce more drag than is necessary. The convection-only model uses a surface temperature distribution that does not change as the design changes. Thus, the convection-only model does not account for the change in surface temperature distribution from the increase in heat sink thickness. Although increasing the thickness of the heat sink increases the thermal resistance in the radial direction, it decreases the thermal resistance in the streamwise direction. Neglecting the decrease in thermal resistance in the streamwise direction caused the convective only model to under-predict the temperature (and thus the heat flux) of the aft portion of the heat sink. Figure 15 shows a comparison between the surface temperatures of convection-only optimized designs using the convection-only and conjugate models. The aft temperature of the convection-only model is lower than the conjugate heat transfer model because the convection-only model does not account for the changes in the conductivity of the heat sink.

The performance of a convection optimized design is comparable to that of the conjugate optimized design with about 50 additional Watts of power. This led to heat exchangers optimized to be larger than necessary in the convection-only case,

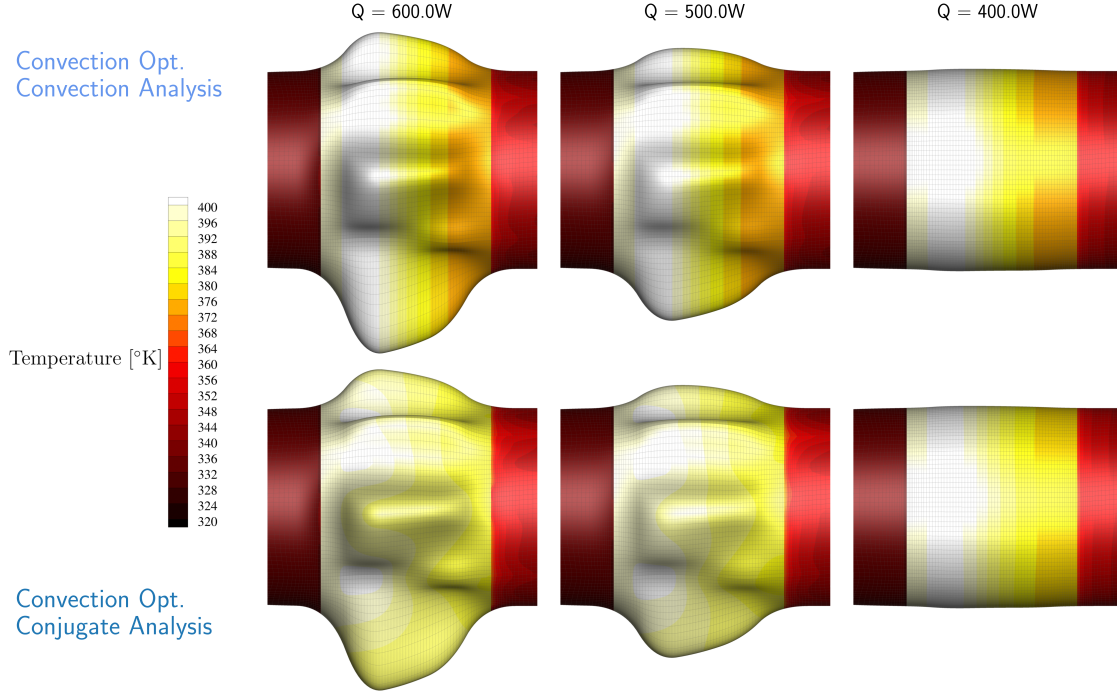


Figure 15: The convection-only model underpredicts the aft temperature of the optimized designs because it does not account for the decrease in thermal resistance of the heat sink in the streamwise direction.

causing more drag. Because the heat exchangers are larger than necessary, they are also heavier than those optimized with a conjugate heat transfer model. The solid blue line in Figure 13 represents the true cooling power of the designs optimized with the convection-only model. Because the underestimation of cooling power is approximately constant in this case, an adjusted convection-only model could be used to arrive at a solution that is almost as good as the optimum of the more expensive conjugate optimization. However, this would require a comparison of the models beforehand and is not necessarily valid for a general problem.

3.1.1 Symmetry

The optimal designs exhibit left-right symmetry but do not always show top-bottom symmetry. Features first appear on the bottom and then extend to the top at higher heat transfer values. We suspect this is caused by the 4° angle of attack used in the cruise condition, making the aerodynamic analysis slightly top-bottom asymmetric. To test this hypothesis, we performed another optimization with a cruise angle of attack of 0° with a heat transfer rate constraint value of 600 W . The results of this optimization show more degrees of symmetry. A comparison of the two shapes and their relative performance at a cruise analysis at 4° angle of attack is shown in Figure 16. Although it was optimized for 0° angle of attack, the design still performs well at 4° angle of attack.

3.2 Comparison of optimal designs and simply designed fins

To compare the finned designs of the optimizer with those of a simpler design, we use the same FFD technique to create designs with 8 and 16 fins. The design with 16 fins required a more refined set of FFD control points to produce. These fin designs were sized to have the same total heat transfer rate as the optimized design, 600 W. Figure 16 shows the drag of these simple fin designs and the designs optimized using the conjugate, conjugate with a cruise angle of attack of 0° , and convective models. The optimized designs have less drag than simply designed fins for the same amount of heat transfer.

Further comparison to designs with even more fins would require further surface mesh refinement. The difference in meshes would obscure the comparison between designs. Furthermore, to analyze a design with over 100 fins, such as the one shown in Figure 1a the required mesh refinement would make the analysis prohibitively expensive to solve, as highlighted in Section 2.7.1. The best way to compare the optimized design with those with many fins is through physical experiments in future work.

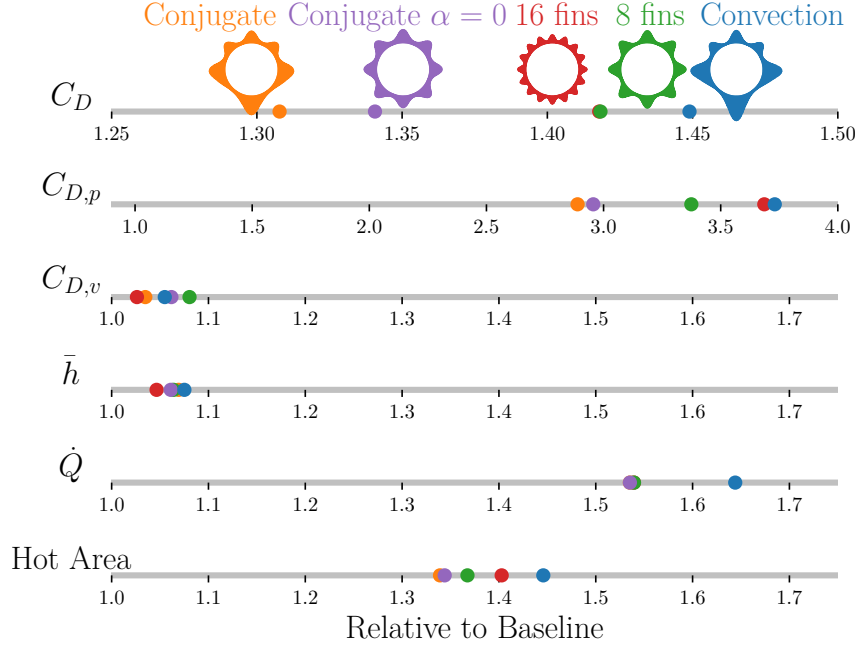


Figure 16: Change in each output relative to the baseline for the conjugate model optimum (orange), conjugate model optimum with 0° cruise angle of attack (purple), convection-only model optimum (blue), a design with 16 fins (red), and a design with 8 fins (green). All designs were sized to reject 600 W.

In all cases, the designs had more heated area and total heat transfer than the baseline design. However, the average heat transfer coefficient did not change much compared to the baseline. The total heat transfer rate is further increased by the rise in aft surface temperature due to the reduction of resistance in the streamwise direction of the heat sink.

The most significant difference between the designs is the pressure drag they produce. Although the viscous drag does vary between designs, it varies over a much smaller range. Consequently, it has a less significant impact on the overall differences in drag. Figure 17 shows a comparison of the streamlines and separation around the designs. The optimized designs have fin profiles that are shifted forwards to reduce the separation on the aft side. This shape change reduces the adverse pressure gradient on the aft side of the optimized fins, which reduces the drag due to the fins. Figure 18 highlights the differences in shape and pressure gradient of the bottom fin for each design.

Increasing the thickness of the forward part of the fins creates a more airfoil-like cross-section because of the parameterization. Adding additional circumferential degrees of freedom to the FFD control points would decouple the fin profile and cross-sectional shape and should be considered for future work.

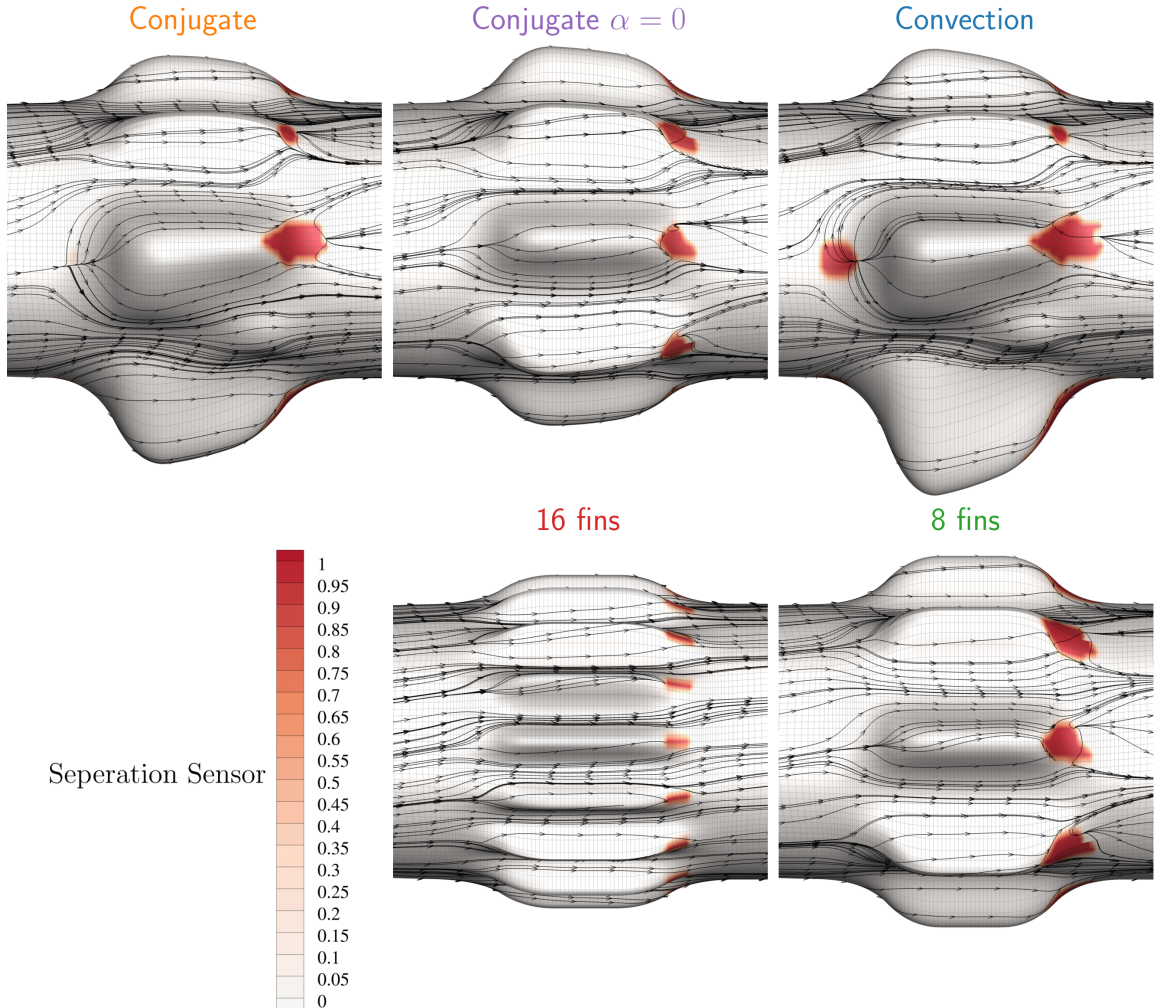


Figure 17: All designs have separated flow aft of the fins (shown in red). If the pressure gradient on the front of the fin is large enough, separation can also occur on the front of the fin.

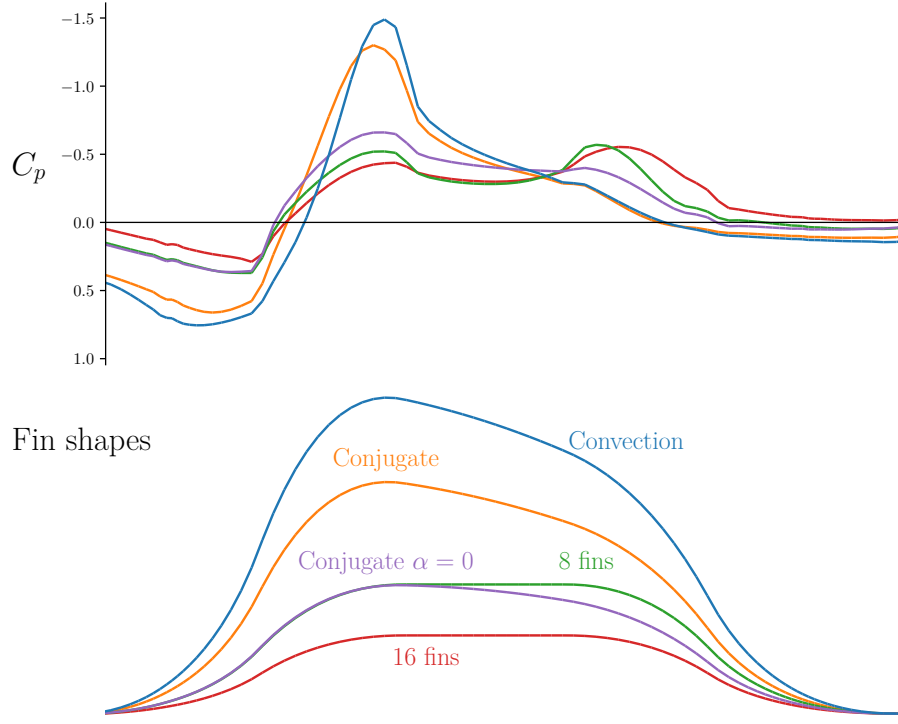


Figure 18: The optimized design fins are tilted forward to lower the adverse pressure gradient and delay separation.

3.2.1 Potential impact of the propeller

The high-pressure regions of the fins will influence the propeller’s performance. However, we expect this effect to be small. Because the propeller’s radius is approximately 3.5 times larger than the largest fin, the fin’s influence would affect a region where little thrust is produced. The swirl of the propeller slipstream will also have an additional impact on the design’s performance. The additional tangential component of velocity will add to the total magnitude of the velocity leading to an increase in the local heat transfer rate. On the other hand, the propeller swirl will also change the angle of the incoming velocity, possibly leading to small regions of separation. The induced tangential velocities are about four to ten times smaller than the induced axial velocities [Stokkermans et al. \(2019\)](#); [Li et al. \(2018\)](#). Thus, we expect the angle of the induced velocity (swirl angle) to remain about 15 degrees or less. During takeoff, the swirl angle will be reduced even further as the freestream velocity adds an additional axial component to the velocity vector. At cruise, the high-lift propellers are not used, and therefore they do not affect the drag of the heat sink at cruise.

4 Conclusions

The thermal management of waste heat is a crucial consideration for electrified aircraft. First-principles-based models can evaluate the performance of novel heat ex-

changers but are too costly to integrate into a manual design loop. Shape optimization alleviates this drawback and provides an automated way to generate high-performance application-specific designs.

We performed aerodynamic shape optimization with both convective and conjugate heat transfer models on the NASA X-57 high-lift motor heat sink with an array of heat transfer constraint values. We used a gradient-based optimizer to solve the optimization problem efficiently. OpenMDAO and MPhys facilitated combining model derivatives into total derivatives and solving the coupled derivative problem.

As the heat load increased, the optimal shape morphed from smooth to finned designs. The designs optimized using a convection-only heat transfer model were larger than necessary because the model underpredicted the heat transfer. The optimized shapes had left-right symmetry but not top-bottom symmetry. When the cruise analysis was modified to be symmetric, the optimal shapes also became top-bottom symmetric. The differences in pressure drag were responsible for most of the drag variation across designs. Compared with simply designed fins, the fins produced by the optimizer had a forward tilt, which reduced the aft separation on the fins and, consequently, drag.

The results presented herein highlight the utility of high-fidelity optimization for heat exchanger design. This methodology facilitates the study of trade-offs in heat exchanger shaping, particularly for new applications such as electric aircraft. Additionally, this methodology could be applied to design heat exchangers in other applications with relatively low heat loads.

Future computational work is needed to parameterize a design space that includes designs with over 100 fins (as shown in Figure 1a) and no fins (as shown in Figure 1b). Furthermore, experimental work is needed to validate the performance of the optimized designs and concretely prove their merit relative to designs with many more fins.

Acknowledgments

The authors would like to acknowledge NASA for providing the funding for this work through grant number F060365 of the Advanced Air Transport Technology (AATT) and Transformational Tools and Technologies (TTT) projects under technical monitor Jeffrey Chin. The computational results of this study were run on the computing resources supplied by the Texas Advanced Computing Center. Furthermore, additional computing resources were provided by the University of Michigan’s Advanced Research Computing Center. The authors would like to acknowledge Graeme Kennedy for his help debugging and using TACS. Furthermore, we would thank Graeme Kennedy and Liam Smith for their development of MeldThermal. We would also like to thank Hannah Hajdik, Alasdair Gray, and Justin Gray for providing feedback on the draft of this paper.

References

- B. Brelje, J. R. R. A. Martins, Electric, hybrid, and turboelectric fixed-wing aircraft: A review of concepts, models, and design approaches, *Progress in Aerospace Sciences*

- 104 (2019) 1–19. doi:[10.1016/j.paerosci.2018.06.004](https://doi.org/10.1016/j.paerosci.2018.06.004).
- J. Welstead, J. L. Felder, Conceptual Design of a Single-Aisle Turboelectric Commercial Transport with Fuselage Boundary Layer Ingestion, in: 54th AIAA Aerospace Sciences Meeting, AIAA SciTech Forum, American Institute of Aeronautics and Astronautics, 2016. doi:[10.2514/6.2016-1027](https://doi.org/10.2514/6.2016-1027).
- S. Stückl, J. van Toor, H. Lobentanzer, Voltair - the all electric propulsion concept platform - a vision for atmospheric friendly flight, in: 28th Congress of the International Council of the Aeronautical Sciences 2012, ICAS 2012, volume 4, Brisbane, Australia, 2012, pp. 2737–2747.
- R. H. Jansen, C. Bowman, A. Jankovsky, R. Dyson, J. Felder, Overview of nasa electrified aircraft propulsion research for large subsonic transports, 53rd AIAA/SAE/ASEE Joint Propulsion Conference, 2017 (2017). doi:[10.2514/6.2017-4701](https://doi.org/10.2514/6.2017-4701).
- M. J. Armstrong, C. A. Ross, M. J. Blackwelder, K. Rajashekara, Trade studies for nasa n3-x turboelectric distributed propulsion system electrical power system architecture, SAE International Journal of Aerospace 5 (2012) 325–336. doi:[10.4271/2012-01-2163](https://doi.org/10.4271/2012-01-2163).
- N. K. Borer, M. D. Patterson, J. K. Viken, M. D. Moore, S. Clarke, M. E. Redifer, R. J. Christie, A. M. Stoll, A. Dubois, J. B. Bevirt, A. R. Gibson, T. J. Foster, P. G. Osterkamp, Design and performance of the nasa sceptor distributed electric propulsion flight demonstrator, in: 16th AIAA Aviation Technology, Integration, and Operations Conference, volume 442, American Institute of Aeronautics and Astronautics Inc, AIAA, 2016, pp. 1–20. doi:[10.2514/6.2016-3920](https://doi.org/10.2514/6.2016-3920).
- R. D. Falck, J. Chin, S. L. Schnulo, J. M. Burt, J. S. Gray, Trajectory optimization of electric aircraft subject to subsystem thermal constraints, in: Proceedings of the 18th AIAA/ISSMO Multidisciplinary Analysis and Optimization Conference, 2017. doi:[10.2514/6.2017-4002](https://doi.org/10.2514/6.2017-4002).
- B. Sundén, J. Fu, Aerospace heat exchangers, Heat Transfer in Aerospace Applications (2017) 89–115. doi:[10.1016/B978-0-12-809760-1.00006-5](https://doi.org/10.1016/B978-0-12-809760-1.00006-5).
- J. W. Chapman, S. L. Schnulo, M. P. Nitzsche, Development of a thermal management system for electrified aircraft, AIAA Scitech 2020 Forum (2020). doi:[10.2514/6.2020-0545](https://doi.org/10.2514/6.2020-0545).
- A. S.A.S., Vahana - our single-seat evtol demonstrator, 2021. URL: <https://www.airbus.com/innovation/zero-emission/urban-air-mobility/vahana.html>.
- E. Sozer, D. Maldonado, K. Bhamidipati, S. L. Schnulo, Computational evaluation of an oml-based heat exchanger concept for HEATheR, in: AIAA Propulsion and Energy 2020 Forum, 2020, pp. 1–22. doi:[10.2514/6.2020-3575](https://doi.org/10.2514/6.2020-3575).

- S. L. Schnulo, J. W. Chapman, P. Hanlon, H. Hasseeb, R. H. Jansen, D. Sadey, E. Sozer, J. Jensen, D. Maldonado, K. Bhamidipati, N. Heersema, K. Antcliff, Z. J. Frederick, J. Kirk, Assessment of the impact of an advanced power system on a turboelectric single-aisle concept aircraft, AIAA Propulsion and Energy 2020 Forum (2020) 1–18. doi:[10.2514/6.2020-3548](https://doi.org/10.2514/6.2020-3548).
- L. Zivan, Eviation Alice all electric aircraft design challenges, 2019. URL: <https://www.youtube.com/watch?v=PWHncSaJQ-A>, electric Aircraft Symposium.
- C. Bentheimer, A. Islami, S. Mainusch, F. Hilpert, B. Eckardt, M. Maerz, Highly efficient sic inverter for aircraft application with innovative thermal management, in: Int. Conf. on Power Conversion and Intelligent Motion, 2019.
- D. L. Hall, J. C. Chin, A. D. Anderson, J. T. Thompson, A. D. Smith, R. D. Edwards, K. P. Duffy, Development of a Maxwell X-57 high lift motor reference design, in: AIAA Propulsion and Energy Forum and Exposition, 2019, American Institute of Aeronautics and Astronautics Inc, AIAA, 2019. doi:[10.2514/6.2019-4481](https://doi.org/10.2514/6.2019-4481).
- H. Kellermann, M. Lüdemann, M. Pohl, M. Hornung, Design and optimization of ram air-based thermal management systems for hybrid-electric aircraft, Aerospace 2021, Vol. 8, Page 3 8 (2020) 3. doi:[10.3390/AEROSPACE8010003](https://doi.org/10.3390/AEROSPACE8010003).
- H. Kellermann, A. L. Habermann, M. Hornung, Assessment of aircraft surface heat exchanger potential, Aerospace 2020, Vol. 7, Page 1 7 (2019) 1. doi:[10.3390/AEROSPACE7010001](https://doi.org/10.3390/AEROSPACE7010001).
- R. K. Shah, D. P. Sekulić, Fundamentals of Heat Exchanger Design, John Wiley & Sons, Inc., 2003.
- W. M. Kays, A. L. London, Compact Heat Exchangers. 3rd Edition, McGraw-Hill, 1998.
- L. Gosselin, M. Tye-Gingras, F. Mathieu-Potvin, Review of utilization of genetic algorithms in heat transfer problems, International Journal of Heat and Mass Transfer 52 (2009) 2169–2188. doi:[10.1016/j.ijheatmasstransfer.2008.11.015](https://doi.org/10.1016/j.ijheatmasstransfer.2008.11.015).
- G. Fabbri, Heat transfer optimization in corrugated wall channels, International Journal of Heat and Mass Transfer 43 (2000) 4299 – 4310. doi:[https://doi.org/10.1016/S0017-9310\(00\)00054-5](https://doi.org/10.1016/S0017-9310(00)00054-5).
- B. H. Dennis, G. S. Dulikravich, I. N. Egorov, S. Yoshimura, Optimization of a large number of coolant passages located close to the surface of a turbine blade, in: American Society of Mechanical Engineers, International Gas Turbine Institute, Turbo Expo (Publication) IGTI, volume 5 A, American Society of Mechanical Engineers Digital Collection, 2003, pp. 13–19. doi:[10.1115/GT2003-38051](https://doi.org/10.1115/GT2003-38051).
- K. Mazaheri, M. Zeinalpour, H. Bokaei, Turbine blade cooling passages optimization using reduced conjugate heat transfer methodology, Applied Thermal Engineering 103 (2016) 1228–1236.

- J. R. R. A. Martins, A. Ning, Engineering Design Optimization, Cambridge University Press, 2022. URL: <https://mdobook.github.io>.
- Y. Yu, Z. Lyu, Z. Xu, J. R. R. A. Martins, On the influence of optimization algorithm and starting design on wing aerodynamic shape optimization, Aerospace Science and Technology 75 (2018) 183–199. doi:[10.1016/j.ast.2018.01.016](https://doi.org/10.1016/j.ast.2018.01.016).
- Z. Lyu, Z. Xu, J. R. R. A. Martins, Benchmarking optimization algorithms for wing aerodynamic design optimization, in: Proceedings of the 8th International Conference on Computational Fluid Dynamics, Chengdu, Sichuan, China, 2014. ICCFD8-2014-0203.
- E. Katamine, S. Mikada, H. Azegami, Shape optimization of steady-state heat-conduction fields considering temperature dependency of thermal conductivity coefficient, Heat Transfer-Asian Research (2013) 364–376. doi:[10.1002/htj.20374](https://doi.org/10.1002/htj.20374).
- Z. P. Wang, S. Turteltaub, M. Abdalla, Shape optimization and optimal control for transient heat conduction problems using an isogeometric approach, Computers and Structures 185 (2017) 59–74. doi:[10.1016/j.compstruc.2017.02.004](https://doi.org/10.1016/j.compstruc.2017.02.004).
- K. Li, X. Qian, Isogeometric analysis and shape optimization via boundary integral, CAD Computer Aided Design 43 (2011) 1427–1437. doi:[10.1016/j.cad.2011.08.031](https://doi.org/10.1016/j.cad.2011.08.031).
- M. Yoon, S. H. Ha, S. Cho, Isogeometric shape design optimization of heat conduction problems, International Journal of Heat and Mass Transfer 62 (2013) 272–285. doi:[10.1016/j.ijheatmasstransfer.2013.02.077](https://doi.org/10.1016/j.ijheatmasstransfer.2013.02.077).
- R. A. Meric, Shape design sensitivity analysis and optimization for nonlinear heat and electric conduction problems, Numerical Heat Transfer; Part A: Applications 34 (1998) 185–203. doi:[10.1080/10407789808913985](https://doi.org/10.1080/10407789808913985).
- S. Kambampati, J. S. Gray, H. A. Kim, Level set topology optimization of heat dissipation devices, in: AIAA Scitech 2019 Forum, June, American Institute of Aeronautics and Astronautics, Reston, Virginia, 2019. doi:[10.2514/6.2019-3558](https://doi.org/10.2514/6.2019-3558).
- M. K. Leader, G. J. Kennedy, Thermoelastic topology optimization using steady-state and transient analysis for stress and thermal performance, AIAA Scitech 2021 Forum (2021) 1–11. doi:[10.2514/6.2021-1895](https://doi.org/10.2514/6.2021-1895).
- T. Dbouk, A review about the engineering design of optimal heat transfer systems using topology optimization, Applied Thermal Engineering 112 (2017) 841–854. doi:[10.1016/j.applthermaleng.2016.10.134](https://doi.org/10.1016/j.applthermaleng.2016.10.134).
- A. Mousavi, S. K. Nadarajah, Heat transfer optimization of gas turbine blades using an adjoint approach, in: 13th AIAA/ISSMO Multidisciplinary Analysis and Optimization Conference 2010, 2010. doi:[10.2514/6.2010-9048](https://doi.org/10.2514/6.2010-9048).

- P. Zhang, J. Lu, L. Song, Z. Feng, Study on continuous adjoint optimization with turbulence models for aerodynamic performance and heat transfer in turbomachinery cascades, *International Journal of Heat and Mass Transfer* 104 (2017) 1069–1082. doi:[10.1016/j.ijheatmasstransfer.2016.08.103](https://doi.org/10.1016/j.ijheatmasstransfer.2016.08.103).
- P. He, J. R. R. A. Martins, C. A. Mader, K. Maki, Aerothermal optimization of a ribbed U-bend cooling channel using the adjoint method, *International Journal of Heat and Mass Transfer* 140 (2019) 152–172. doi:[10.1016/j.ijheatmasstransfer.2019.05.075](https://doi.org/10.1016/j.ijheatmasstransfer.2019.05.075).
- C.-Z. Wang, K. R. Nagisetty, F. Montanari, D. C. Hill, Application of adjoint solver to optimization of fin heat exchanger, in: *ASME Turbo Expo 2015: Turbine Technical Conference and Exposition*, American Society of Mechanical Engineers, 2015.
- K. Gkaragkounis, E. Papoutsis-Kiachagias, K. Giannakoglou, The continuous adjoint method for shape optimization in conjugate heat transfer problems with turbulent incompressible flows, *Applied Thermal Engineering* 140 (2018) 351–362. doi:[10.1016/j.applthermaleng.2018.05.054](https://doi.org/10.1016/j.applthermaleng.2018.05.054).
- P. Mario, K. Tsuguo, F. Kenichiro, Optimization of fin topology for heat transfer within lightweight plate-fin heat exchangers, *Journal of Thermophysics and Heat Transfer* (2021) 1–9. doi:[10.2514/1.T6121](https://doi.org/10.2514/1.T6121).
- A. Mousavi, S. Nadarajah, Adjoint-based multidisciplinary design optimization of cooled gas turbine blades, *American Institute of Aeronautics and Astronautics (AIAA)*, 2011. doi:[10.2514/6.2011-1131](https://doi.org/10.2514/6.2011-1131).
- A. Racca, T. Verstraete, L. Casalino, Radial turbine thermo-mechanical stress optimization by multidisciplinary discrete adjoint method, *International Journal of Turbomachinery, Propulsion and Power* 5 (2020) 30. doi:[10.3390/ijtp5040030](https://doi.org/10.3390/ijtp5040030).
- R. Sandboge, D. I. Papadimitriou, M. P. Reddy, Shape and topology optimization in computational fluid dynamics including heat transfer using gaussian processes and adjoint methods, in: *AIAA Scitech 2021 Forum*, American Institute of Aeronautics and Astronautics Inc, AIAA, 2021, pp. 1–23. doi:[10.2514/6.2021-1892](https://doi.org/10.2514/6.2021-1892).
- K. T. Gkaragkounis, E. M. Papoutsis-Kiachagias, A. G. Tsolovikos, K. C. Giannakoglou, Effect of grid displacement models on sensitivity derivatives computed by the continuous adjoint method i aerodynamic and conjugate heat transfer shape optimization, *Engineering Optimization* (2020) 1–19. doi:[10.1080/0305215X.2020.1796998](https://doi.org/10.1080/0305215X.2020.1796998).
- K. T. Gkaragkounis, E. M. Papoutsis-Kiachagias, K. C. Giannakoglou, Adjoint-assisted pareto front tracing in aerodynamic and conjugate heat transfer shape optimization, *Computers and Fluids* 214 (2021) 104753. doi:[10.1016/j.compfluid.2020.104753](https://doi.org/10.1016/j.compfluid.2020.104753).
- E. M. Papoutsis-Kiachagias, K. C. Giannakoglou, An adjoint-based topology optimization framework for fluid mechanics and conjugate heat transfer in openfoam, in: *8th OpenFOAM Conference*, Digital Event, Taylor and Francis, 2020, pp. 1–11.

- D. S. Makhija, P. S. Beran, Concurrent shape and topology optimization for steady conjugate heat transfer, *Structural and Multidisciplinary Optimization* 59 (2019) 919–940. doi:[10.1007/s00158-018-2110-4](https://doi.org/10.1007/s00158-018-2110-4).
- J. L. Anibal, C. A. Mader, J. R. R. A. Martins, Aerothermal optimization of X-57 high-lift motor nacelle, in: *AIAA SciTech Forum*, AIAA, Orlando, FL, 2020. doi:[10.2514/6.2020-2115](https://doi.org/10.2514/6.2020-2115).
- J. S. Gray, J. T. Hwang, J. R. R. A. Martins, K. T. Moore, B. A. Naylor, OpenMDAO: An open-source framework for multidisciplinary design, analysis, and optimization, *Structural and Multidisciplinary Optimization* 59 (2019) 1075–1104. doi:[10.1007/s00158-019-02211-z](https://doi.org/10.1007/s00158-019-02211-z).
- N. Wu, G. Kenway, C. A. Mader, J. Jasa, J. R. R. A. Martins, pyOptSparse: a Python framework for large-scale constrained nonlinear optimization of sparse systems, *Journal of Open Source Software* 5 (2020) 2564. doi:[10.21105/joss.02564](https://doi.org/10.21105/joss.02564).
- N. Secco, G. K. W. Kenway, P. He, C. A. Mader, J. R. R. A. Martins, Efficient mesh generation and deformation for aerodynamic shape optimization, *AIAA Journal* 59 (2021) 1151–1168. doi:[10.2514/1.J059491](https://doi.org/10.2514/1.J059491).
- A. B. Lambe, J. R. R. A. Martins, Extensions to the design structure matrix for the description of multidisciplinary design, analysis, and optimization processes, *Structural and Multidisciplinary Optimization* 46 (2012) 273–284. doi:[10.1007/s00158-012-0763-y](https://doi.org/10.1007/s00158-012-0763-y).
- C. A. Mader, G. K. W. Kenway, A. Yildirim, J. R. R. A. Martins, ADflow: An open-source computational fluid dynamics solver for aerodynamic and multidisciplinary optimization, *Journal of Aerospace Information Systems* 17 (2020) 508–527. doi:[10.2514/1.I010796](https://doi.org/10.2514/1.I010796).
- G. K. W. Kenway, C. A. Mader, P. He, J. R. R. A. Martins, Effective adjoint approaches for computational fluid dynamics, *Progress in Aerospace Sciences* 110 (2019) 100542. doi:[10.1016/j.paerosci.2019.05.002](https://doi.org/10.1016/j.paerosci.2019.05.002).
- A. Yildirim, G. K. W. Kenway, C. A. Mader, J. R. R. A. Martins, A Jacobian-free approximate Newton–Krylov startup strategy for RANS simulations, *Journal of Computational Physics* 397 (2019) 108741. doi:[10.1016/j.jcp.2019.06.018](https://doi.org/10.1016/j.jcp.2019.06.018).
- K. A. Deere, S. A. Viken, M. B. Carter, J. K. Viken, J. M. Derlaga, A. M. Stoll, Comparison of high-fidelity computational tools for wing design of a distributed electric propulsion aircraft, in: *35th AIAA Applied Aerodynamics Conference*, AIAA Paper 2017-3925, AIAA, 2017. doi:[10.2514/6.2017-3925](https://doi.org/10.2514/6.2017-3925).
- S. L. Schnulo, D. L. Hall, J. C. Chin, A. D. Smith, Further development of the NASA X-57 Maxwell mission planning tool for mods ii, iii, and iv, in: *AIAA Propulsion and Energy Forum and Exposition*, 2019, American Institute of Aeronautics and Astronautics Inc, AIAA, 2019. doi:[10.2514/6.2019-4491](https://doi.org/10.2514/6.2019-4491).

- D. C. Deisenroth, M. Ohadi, Thermal management of high-power density electric motors for electrification of aviation and beyond, *Energies* 2019, Vol. 12, Page 3594 12 (2019) 3594. doi:[10.3390/EN12193594](https://doi.org/10.3390/EN12193594).
- T. Verstraete, The VKI U-Bend Optimization Test Case, Technical Report, 2016. URL: <http://aboutflow.sems.qmul.ac.uk/events/munich2016/benchmark/testcase1/>.
- E. Divo, E. Steinthorsson, F. Rodriquez, A. Kassab, J. Kapat, J. Heidmann, Glenn-HT/BEM conjugate heat transfer solver for large-scale turbomachinery models, NASA Technical Memorandum R—2003- (2003). URL: <https://ntrs.nasa.gov/citations/20040000109>.
- T. Verstraete, S. Scholl, Stability analysis of partitioned methods for predicting conjugate heat transfer, *International Journal of Heat and Mass Transfer* 101 (2016) 852–869. doi:[10.1016/j.ijheatmasstransfer.2016.05.041](https://doi.org/10.1016/j.ijheatmasstransfer.2016.05.041).
- G. J. Kennedy, J. R. R. A. Martins, A parallel finite-element framework for large-scale gradient-based design optimization of high-performance structures, *Finite Elements in Analysis and Design* 87 (2014) 56–73. doi:[10.1016/j.finel.2014.04.011](https://doi.org/10.1016/j.finel.2014.04.011).
- J. F. Kiviaho, G. J. Kennedy, Efficient and Robust Load and Displacement Transfer Scheme Using Weighted Least Squares, Technical Report 5, 2019. doi:[10.2514/1.J057318](https://doi.org/10.2514/1.J057318).
- L. J. Smith, L. J. Halim, G. J. Kennedy, M. J. Smith, A high-fidelity coupling framework for aerothermoelastic analysis and adjoint-based gradient evaluation, in: *AIAA Scitech 2021 Forum*, American Institute of Aeronautics and Astronautics Inc, AIAA, 2021. doi:[10.2514/6.2021-0407](https://doi.org/10.2514/6.2021-0407).
- J. R. R. A. Martins, J. T. Hwang, Review and unification of methods for computing derivatives of multidisciplinary computational models, *AIAA Journal* 51 (2013) 2582–2599. doi:[10.2514/1.J052184](https://doi.org/10.2514/1.J052184).
- J. T. Hwang, J. R. R. A. Martins, A computational architecture for coupling heterogeneous numerical models and computing coupled derivatives, *ACM Transactions on Mathematical Software* 44 (2018) Article 37. doi:[10.1145/3182393](https://doi.org/10.1145/3182393).
- J. R. R. A. Martins, J. J. Alonso, J. J. Reuther, A coupled-adjoint sensitivity analysis method for high-fidelity aero-structural design, *Optimization and Engineering* 6 (2005) 33–62. doi:[10.1023/B:OPTE.0000048536.47956.62](https://doi.org/10.1023/B:OPTE.0000048536.47956.62).
- O. Burghardt, N. R. Gauger, P. Gomes, R. Palacios, T. Kattmann, T. D. Economon, coupled discrete adjoints for multiphysics in SU2, in: *AIAA AVIATION 2020 FORUM*, volume 1 PartF, American Institute of Aeronautics and Astronautics Inc, AIAA, 2020. doi:[10.2514/6.2020-3139](https://doi.org/10.2514/6.2020-3139).

- J. R. R. A. Martins, P. Sturdza, J. J. Alonso, The complex-step derivative approximation, *ACM Transactions on Mathematical Software* 29 (2003) 245–262. doi:[10.1145/838250.838251](https://doi.org/10.1145/838250.838251).
- T. W. Sederberg, S. R. Parry, Free-form deformation of solid geometric models, *SIGGRAPH Comput. Graph.* 20 (1986) 151–160. doi:[10.1145/15886.15903](https://doi.org/10.1145/15886.15903).
- A. Dubois, M. van der Geest, J. Bevirt, R. Christie, N. K. Borer, S. C. Clarke, Design of an electric propulsion system for sceptor’s outboard nacelle, 16th AIAA Aviation Technology, Integration, and Operations Conference (2016). doi:[10.2514/6.2016-3925](https://doi.org/10.2514/6.2016-3925).
- P. E. Gill, W. Murray, M. A. Saunders, SNOPT: An SQP algorithm for large-scale constrained optimization, *SIAM Journal of Optimization* 12 (2002) 979–1006. doi:[10.1137/S1052623499350013](https://doi.org/10.1137/S1052623499350013).
- G. K. W. Kenway, J. R. R. A. Martins, Buffet-onset constraint formulation for aerodynamic shape optimization, *AIAA Journal* 55 (2017) 1930–1947. doi:[10.2514/1.J055172](https://doi.org/10.2514/1.J055172).
- T. C. A. Stokkermans, N. van Arnhem, T. Sinnige, L. L. M. Veldhuis, Validation and comparison of RANS propeller modeling methods for tip-mounted applications, *AIAA Journal* 57 (2019) 566–580. doi:[10.2514/1.J057398](https://doi.org/10.2514/1.J057398).
- Q. Li, K. Öztürk, T. Sinnige, D. Ragni, G. Eitelberg, L. Veldhuis, Y. Wang, Design and experimental validation of swirl-recovery vanes for propeller propulsion systems, *AIAA Journal* 56 (2018) 4719–4729. doi:[10.2514/1.J057113](https://doi.org/10.2514/1.J057113).